Size and shape effect in the pull-out of FRP reinforcement from concrete

Gaia Barbieri *, Luigi Biolzi, Massimiliano Bocciarelli, Sara Cattaneo

Department of Architecture, Built Environment and Construction Engineering – ABC, Politecnico di Milano, Piazza Leonardo da Vinci 32, 20133 Milano, Italy

Scaling phenomena in the progressive debonding between fiber reinforced polymer (FRP) strips and con-crete substrate are examined on the basis of single lap shear tests, considering different bond lengths and widths. To capture a stable post-peak response of the FRP-concrete joint, the slip between the concrete support and the reinforcement strip, measured at the reinforcement end using a clip gage, was selected as feedback control signal during the tests. This allowed a quasi-static stable fracture propagation in the descending branch until complete load relaxation and debonding. Experimental tests were simulated by means of 2D and 3D finite element analyses adopting two different approaches. At first, a numerical model based on linear elastic materials with all non-linearities concentrated at the interface was assumed. It clearly revealed the inability to recognize all the aspects of the debonding process. Then, a different numerical model, based on a non-linear constitutive model for concrete and perfect adhesion between all the materials, was adopted.

Keywords: Carbon fiber, Debonding, Fracture, Finite element analysis (FEA), Width effect

1. Introduction

An encouraging technique to enhance the mechanical performance of masonry or concrete structures by strengthening or stiffening a member, is to apply strips of fiber reinforced polymer (FRP) [1–5]. FRPs are versatile materials, with widely varying mechanical and physical properties dependent on the constituents as well as fabrication and processing conditions. Typically, an FRP is characterized by high strength-to-weight ratio, corrosion resistance, durability and versatility, allowing its use in a broad range of applications. Although some concerns exist related to long-term performance and failure modes, the application of FRPs represents a viable solution for many projects.

One of the most important effects influencing the composite structural behavior is the interfacial stress transfer, including debonding. In pull-out tests the axial force in the strip is gradually transmitted to the substrate by shear forces acting at the interface. Such stresses decay with a high gradient, passing from the loaded end to the free one of the strip, so that they can be assumed to be active on a definite length only, usually denoted as effective bond length or effective stress transfer length. In long strips, as the load increases, debonding near the applied load shifts the stress transfer zone to new areas farther away from the loading point, confirming that only part of the bond is active in the forces transmission. Thus, the joint strength does not increase with an increase of the bond length beyond its active value. The entire debonding process of FRP-to-concrete bonded joints is described in [6]. Experiments reveal that the recurrent failure mode in a "pull" test on a specimen with a bonded FRP plate is shear failure of the concrete, typically within millimeters from the concrete-to-adhesive interface [7]. This was also observed in more general terms in [8] by the analysis of brittle substrates beneath adherent films. Therefore, to capture the real response of the joint under a loading history, numerical and/or theoretical approaches have to account for the nonlinear material concrete properties and debonding cannot be always confined at the interface between the FRP strip and concrete substrate. In addition, because of microcracking and fracture in concrete due to the high stress gradients arising in the joints, the experimental results are affected by size effect.

Many studies dealt with the prediction of the ultimate load and the definition of a proper bond–slip law and an effective bond length. They may be classified into three broad categories: (i) empirical models based on the regression of test data, e.g. [9,10], (ii) fracture-mechanics-based models, e.g. [6,11–15], (iii) numerical-methods-based models, e.g. [16–21].

While an understanding of the influence of the bond length on the ultimate load is emerging, less attention has been paid to the role played by the widths of concrete and FRP on the ultimate load and debonding process.

In some studies, the relationship between the width and the maximum load has been translated into a geometrical factor, assumed also by some national and international recommendations, e.g. [22,23], obtained by empirical equations resulting from

Article history:
Available online 4 February 2016

* Corresponding author. Tel.: +39 0223999481.
E-mail address: barbierigaia@gmail.com (G. Barbieri).

Published Journal Article available at: http://dx.doi.org/10.1016/j.compstruct.2016.01.097

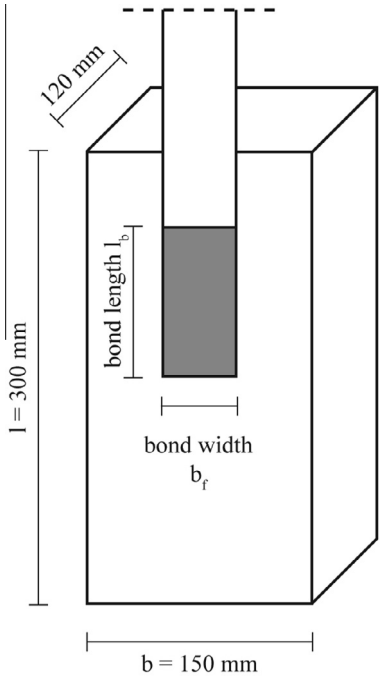

Fig. 1. Configurations for reinforced specimens.

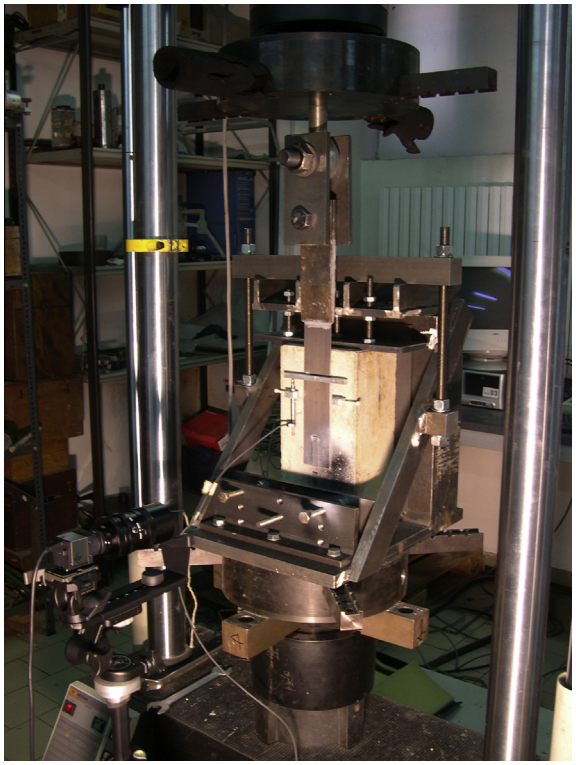

Fig. 2. Experimental setup for single shear lap test.

Table 1
Concrete properties.

Test	Strength [MPa]
Cube resistance (21 days), $R_{cm,21}$	32.40
Cube resistance (28 days), $R_{cm,28}$	36.30
Cylindrical resistance (21 days), $f_{cm,21}$	26.90
Cylindrical resistance (28 days), $f_{cm,28}$	32.59
Brazilian splitting test (28 days), f_{ctm}	2.88

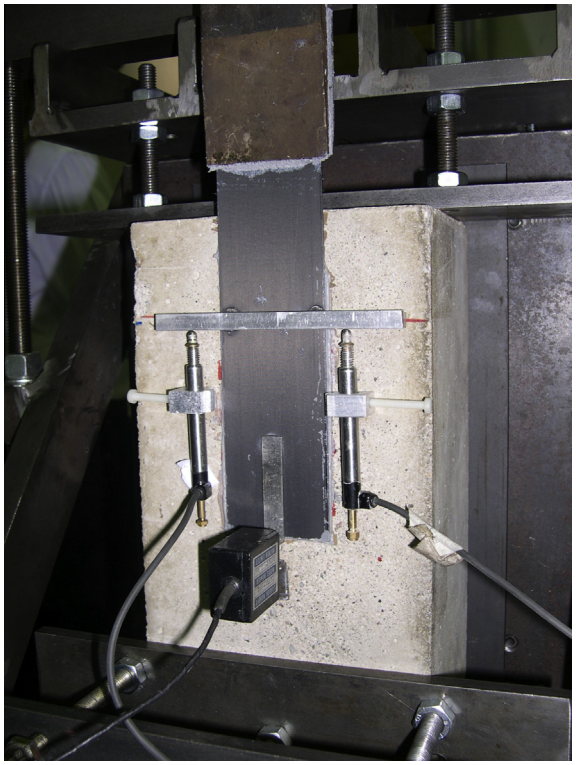

Fig. 3. Point sensors (LVDTs and a clip gage) monitoring relative displacements between the reinforcement and concrete.

regression analyses of experimental data [11,12,18,19,24,25]. The introduction of such a factor implies to consider the debonding problem as a bi-dimensional one. Indeed, in the early studies, numerical models of FRP/concrete systems were assumed to be in plane stress state and the effect of different widths was studied only introducing such a geometrical factor [20,21,26]. However, the experimental push–pull tests collected by several Authors that have investigated the influence of the FRP width [7,18,27–29] have clearly shown that this parameter is a decisive issue. The tests performed with this specific goal are rather scarce. In addition, it is often very difficult to compare the results due to the fact that even considering tests with the same bonded length and width, the thickness of the reinforcement, the concrete resistance, the dimension of the specimen, which play an important role on strength of the joint, are different. Some of the data collected show significant contradictions between what is experimentally observed and what the standards provide [18,27,28]. Although these studies do not present a complete discussion on the influence of the FRP width on the strength of the system, they surely highlight that the debonding phenomena is essentially a tri-dimensional problem, where, due to the different mechanical properties of the materials, the width effect has an important role on the stress distribution in concrete and on the failure mechanism occurring [30]. Currently, three-dimensional numerical investigations of these phenomena are presented in very few studies, e.g. [30–33]. In addition, some researchers have recently introduced the concept of effective bond width, that take into account the contribution of a thin concrete layer external to the bonded area in the fracture process [30].

Table 2
Single shear test data.

Specimen #		Bond length l_b [mm]	Width b_f [mm]	1st peak load $F_{1st\ peak}$ [kN]	Failure load F_{max} [kN]
25	1L	25	25	–	4.13
	2L	25	25	–	3.70
50	1W	50	25	–	7.57
	2W	50	50	14.67	17.10
100	1W	100	50	24.54	27.48
	2W	100	100	45.62	46.28
150	1L	150	50	26.13	28.35
	2L	150	50	25.00	25.18
	3L	150	50	19.54	21.54
200	1L	200	50	–	27.54
	2L	200	50	26.44	26.88
	3L	200	50	–	25.64

In this paper, the influence of the width of the CFRP reinforcement on the stress field and on the load carrying capacity is discussed for single lap shear push–pull configuration, by means of both experimental tests and numerical analyses. Different bond lengths and widths strips were considered in order to evaluate their effects on the joint strength. At first, the experimental campaign is described. The tests, initially controlled by the loaded edge displacement and subsequently, at the onset of the debonding process, by a clip gage mounted at the end of the reinforcement, are presented. A stable quasi-static fracture propagation and the entire debonding of the reinforcement from the concrete support, were captured even in the post-peak with snap-back softening branches. A formation of a concrete bulb at the end of the reinforcement, that influences the maximum load transmitted by the joint as well as the damage mechanisms, was observed. A numerical investigation was conducted using different finite element models in order to interpreter the experimental observations. Initially, both 2D and 3D analyses were performed, in which failure was assumed to occur at the interface, by adopting linear elastic materials and zero-thickness interface elements endowed with a non-linear cohesive law. By means of a Riks procedure it was possible to capture the post-peak snap-back behavior due to the failure process and to compare experimental and numerical results in terms of overall response of the system. In addition, different 3D finite element analyses were performed by means of a numerical model based on a non-linear constitutive model for concrete and a perfect adhesion between all the materials involved. The development of the damage, the formation of the resistant bulb and the width effects of the reinforcement on the joint strength were analyzed as a consequence of a complex tri-dimensional stress field strongly affected by the test configuration.

2. Experimental techniques

2.1. Specimens preparation and mechanical properties of the materials

CFRP laminates, with different widths b_f and bond lengths l_b were externally glued to prismatic concrete specimens, 150 × 300 × 120 mm ($b \times l \times h$), as shown in Fig. 1.

The concrete specimens were composed of the following mix: Portland cement CEM I 52.5 R according to the ENV 197/1 European standard, natural river aggregate with a maximum size of 25 mm, aggregate/binder ratio of 5, and a water/binder ratio of 0.7. All specimens were prepared using steel molds and consolidated with a high frequency vibrating table, removed from the mold after 24 h, and cured in water at a temperature of 20 °C for 1 week and in air (20 °C and 90% R.H.) for 3 weeks.

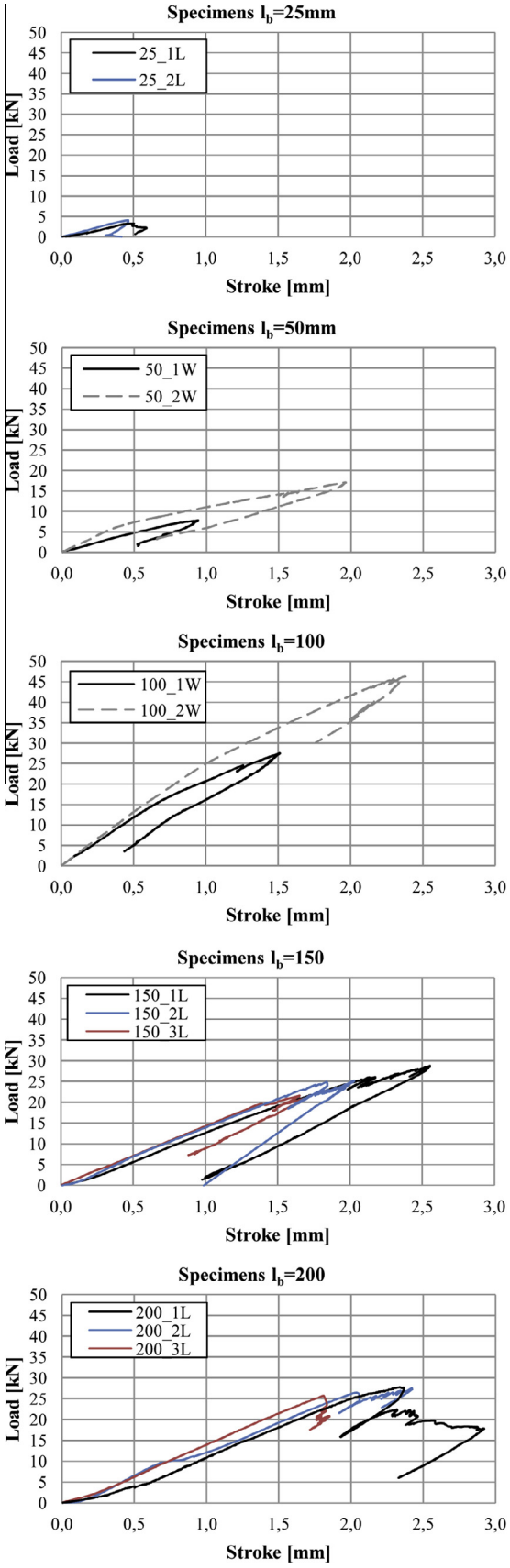

Fig. 4. Load–stroke curves.

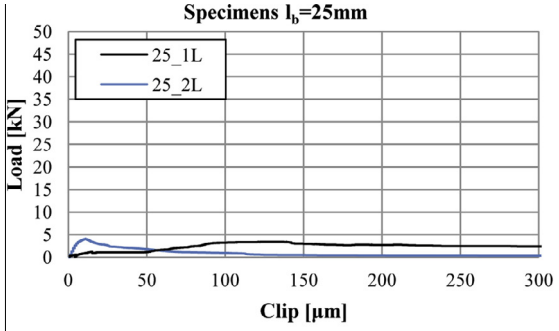

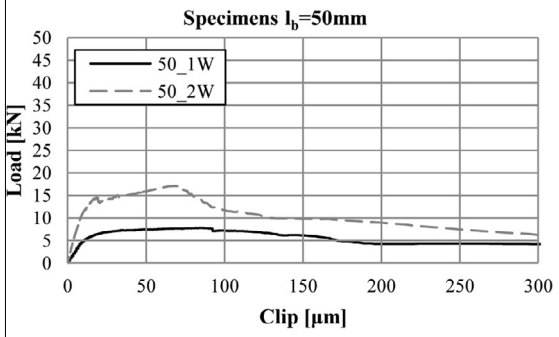

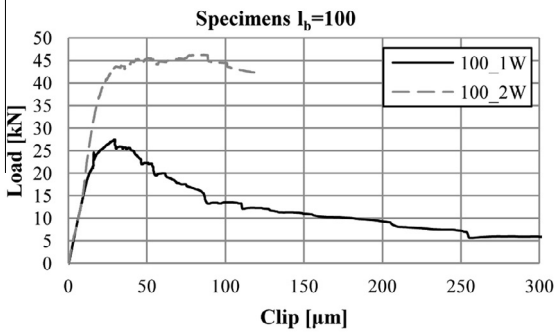

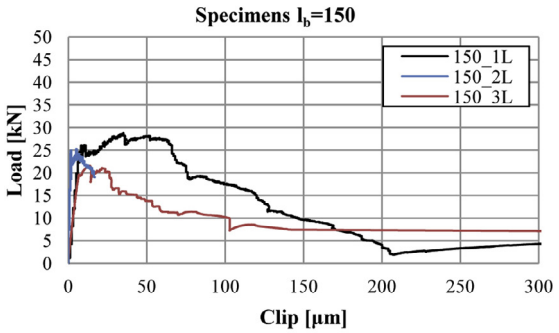

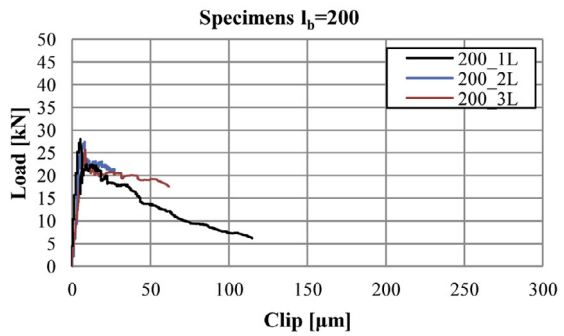

Fig. 5. Load–clip gages displacement curves.

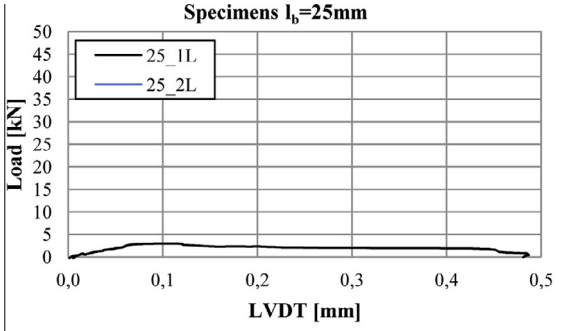

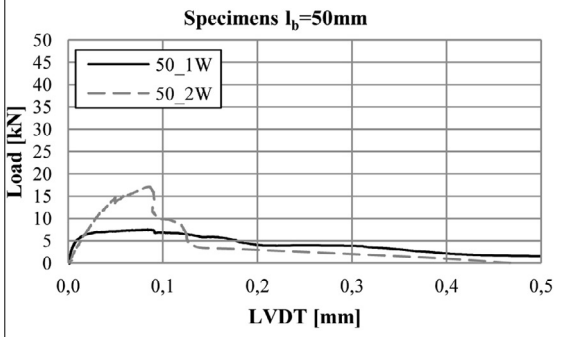

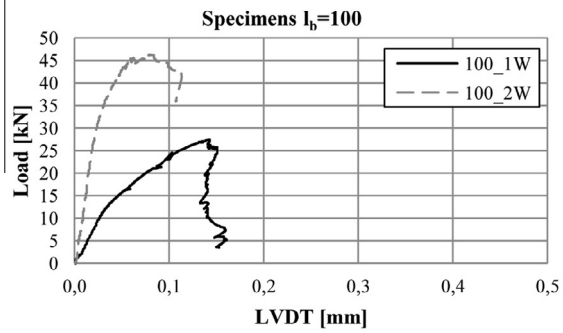

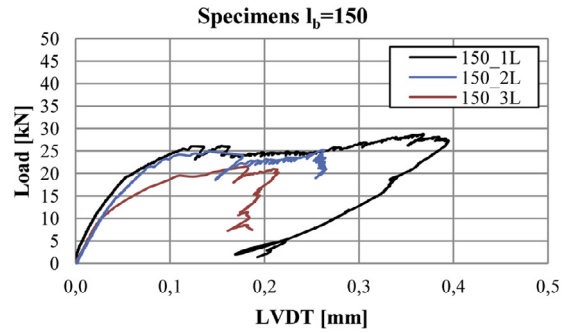

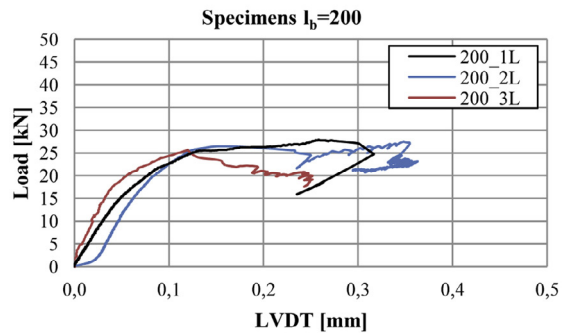

Fig. 6. Load–LVDT displacement curves.

Fig. 7. Bulb at FRP anchorage, for different size and shape of the bonded area.

The compressive strength was evaluated at 21 and 28 days on both cubes (side 150 mm) and cylinders (diameter 100 mm, height 200 mm) and the tensile strength was obtained by splitting test. The average values of cube compressive strength R_{cm}, cylindrical compressive strength f_{cm} and tensile strength f_{ctm}, were obtained by five tests and are reported in Table 1. Young modulus E_c, determined from the uniaxial compression tests, was 30.5 GPa.

A carbon fiber reinforced polymer (CFRP) with a thickness t_f of 1.4 mm was used. The material properties of the laminate were: tensile strength f_f greater than 3.1 GPa, Young modulus E_f equal to 170 GPa, Poisson ratio v_f of 0.20 and strain to failure ε_{fu} of 2%. The ultimate force per unit width of FRP and the stiffness per unit width were computed to be equal to 43.4 kN/cm and 2380 kN/cm, respectively.

Epoxy resin was characterized by a 6.0 GPa Young modulus and a 0.30 Poisson ratio.

2.2. Experimental setup

The testing system consisted of a closed-loop electromechanical Instron load frame with a maximum capacity of 100 kN (Fig. 2). The main characteristics are as follows:

(i) Electromechanical control with a minimum speed of 2 μm/h.
(ii) Three control channels, one of which can be external (giving the possibility to choose the feedback signal that allows a stable test control).
(iii) Closed-loop control with integral and derivative gain (in order to remove the effect of the finite stiffness of the machine).

The specimen was fixed by means of a steel support designed to reduce the elastic rotation, i.e. the deformation of the support and of the specimen. The supporting steel plates were controlled by bolts, which permitted reduction in geometrical eccentricities by regulating the specimen arrangement. The alignment was checked with an electronic digital caliper with accuracy 0.02 mm. The end of the CFRP laminate subjected to traction was clamped within two steel plates compressed by bolts. To capture the post-peak behavior of the system even with snap-back softening branch, the tests were performed in a servo-controlled load frame, with a strain gage transducer (clip gage), positioned at 10 mm from the free end of the reinforcement, that measured the relative slip

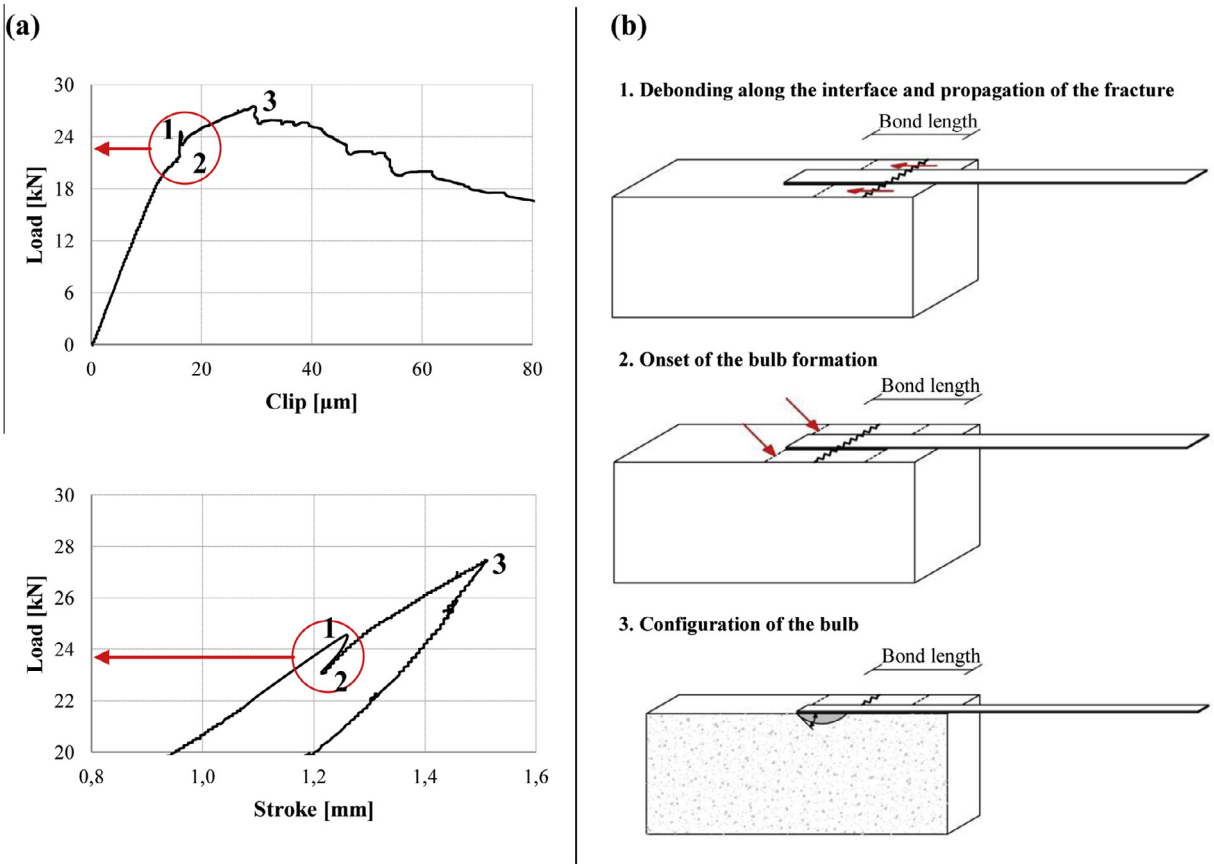

Fig. 8. Onset e propagation of the bulb. Specimen with bond length 100 mm and width 50 mm.

Fig. 9. Experimental evidence of the bulb formation.

between the CFRP strip and the substrate, as monotonously increasing feedback signal. In addition, two LVDTs measured the relative displacement between the concrete and the composite at the beginning of the bonded area (at a distance around 25 mm), see Fig. 3.

The tests were started in stroke control at a rate of 0.01 μm/s until the displacement measured by the clip gage registered some displacements (of the order of 10 μm). Then the control was switched to the clip gage with a rate of 0.01 μm/s, which was increased in the final phase of debonding. In this way, even with a very brittle response of a joint, it was possible to follow stable propagation of fracture.

3. Experimental results

Bond length and width of all configurations experimentally tested are reported in Table 2. All the experimental curves obtained were characterized by a snap-back behavior in stroke (Fig. 4). Figs. 5 and 6 show the load–clip gages displacement and the load–LVDT displacement curves, respectively. As it is possible to observe, the maximum load was higher for the longer and the wider FRP reinforcement.

Analyzing Fig. 4, it is clear that the mechanical response in most of the tests with bond length greater than 25 mm is initially linear, and subsequently a non-linear behavior is observed up to an instantaneous load drop (first peak). Following this drop, the load increases to reach a maximum value at failure (second peak). A summary of the experimental results is given in Table 2.

Due to the capability of experimental procedure to follow the entire debonding process, also in the softening branch, the formation of a bulb at the end of the reinforcement was observed clearly in almost all tests [34,35] (Fig. 7). The extension of such a bulb was approximately equal to the width of the strip, and it seemed not dependent on the reinforcement length. It was possible to identify the onset of the bulb formation by comparing the load–stroke and the load–clip curves of the individual tests: considering e.g. the specimen characterized by 100 mm bond length and 50 mm width, Fig. 8a shows that when the load drops with a small change in clip gage displacement, the load–stroke response exhibited an unstable branch (snap-back). Therefore, it was noted that the development of the bulb seemed allow the system to reach a higher maximum force, which corresponds to the second peak of the curve. In addition, the onset of the bulb is due to peeling stresses at the free edge of the reinforcement [36]. These stresses are normal to the interface along which the reinforcement is attached to concrete and, combined with the shearing stresses (tangent to the interface), produce a resultant that is roughly perpendicular to the fracture surface showed in Fig. 9.

The formation of the resistant bulb was the consequence of the competition of two damage mechanisms in the system, that is (Fig. 8b):

i Debonding along the interface (mode-II), starting from the loaded end and affecting few millimeters of the concrete surface.
ii Mixed-mode fracture starting at the free end and propagating along a path, about 30° inclined, with the formation of the bulb.

4. Numerical modeling with non-linear properties in interface

The fracture tests were simulated adopting both 2D plane stress and 3D finite element models implemented in the code Abaqus [37]. A Riks procedure was adopted to follow the post-failure snap-back branch of the joint response.

The experimental setup was simulated constraining the lower edge (2D) or face (3D) in vertical direction and 3/4 of the right edge (2D) or face (3D) in horizontal one, starting from the bottom. To reduce the degrees of freedom of the numerical problem, in the 3D model symmetry conditions were exploited, as shown in Fig. 10. The loading consisted of an increasing displacement

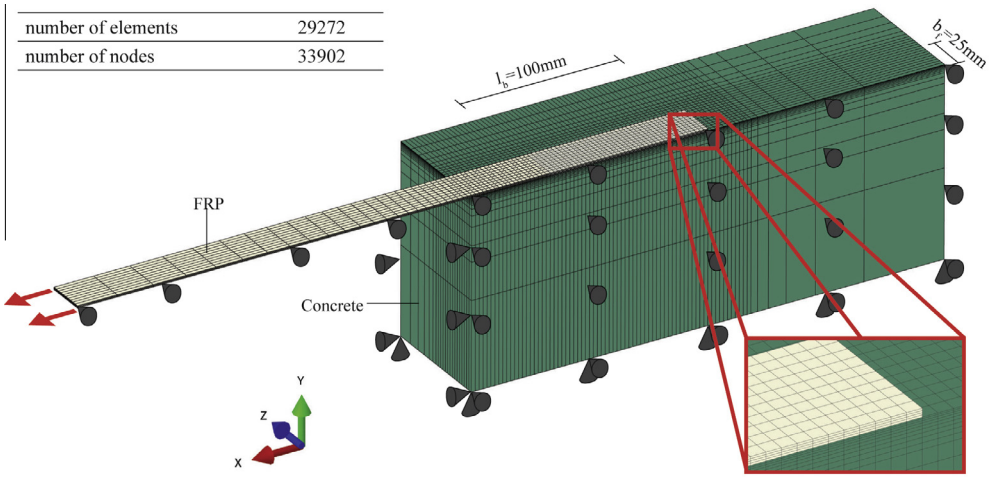

Fig. 10. Geometry, constraints, loading conditions and discretization of the 3D numerical model with 100 mm bond length and 50 mm FRP width.

applied at the loaded end of the FRP strip. Linear quadrilateral elements and 8-node linear bricks were adopted for 2D and 3D models, respectively. Zero-thickness interface elements were inserted between concrete substrate and FRP, to take into account the non-linear behavior of the interface, by means of user's defined routines (UEL) implemented in Abaqus and endowed with a proper cohesive law described in Section 4.1. FRP strip and concrete were assumed linear elastic with the mechanical properties reported in Table 1. The mesh was refined where higher stress gradient, damage and crack phenomena were expected.

Fig. 10 shows the geometry, constraints, loading conditions and discretization of the 3D numerical model with 100 mm bond length and 50 mm FRP width, with a zoom in the areas close to the end of the specimen.

4.1. Cohesive model

Cohesive laws regard fracture as a gradual separation between two surfaces resisted by cohesive tractions which the two surfaces exchange and which are assumed to be function of the opening/sliding displacements.

In literature, many theoretical models in terms of shear stress versus interface slip were developed for the case of concrete supports, based on observed experimental behavior of strengthened components. The existing most popular bond–slip models are: (i) linear brittle models, e.g. [16], (ii) bilinear model, e.g. [11,18,22,24], (iii) exponential models, e.g. [38,39].

It is well known that the role played in the numerical simulations by the shape of the cohesive law is marginal compared to the role played by the peak of the curve, i.e. the interface strength, and the area under it, i.e. the fracture energy. The exponential cohesive law originally proposed in [40], and then used for instance, for CFRP reinforced steel and masonry specimens [41–43], was adopted in this study.

Assuming w as a scalar measure of the displacement jump vector across the interface, the non-holonomic behavior of the interface model is governed by the maximum attained effective interface jump w_{max}, which represents the only internal variable of the model:

$$w = \sqrt{\beta^2 s^2 + \delta^2}$$
$$\dot{w}_{max} = \begin{cases} \dot{w} & \text{if} \quad w = w_{max} \text{ and } \dot{w} \geqslant 0 \\ 0 & \text{otherwise} \end{cases} \tag{1}$$

where β is a parameter assigning different weights to the sliding, s, and opening, δ, relative displacement components.

Under progressive debonding, the response of the cohesive interface is characterized by a shear stress which increase up to the maximum value τ_f and then it decrease asymptotically to zero in the softening regime. Cohesive tractions are obtained by derivatives of the free energy density function φ defined in, e.g. [41], with respect to the relative displacements, while a linear path back to the origin is assumed during unloading, therefore:

$$\begin{cases} \sigma_n = \frac{\partial \varphi}{\partial \delta} = \frac{\sigma_f}{w_c} e^{\left(1-\frac{w}{w_c}\right)} \delta \\ \tau_s = \frac{\partial \varphi}{\partial s} = \frac{\tau_f}{w_c} e^{\left(1-\frac{w}{w_c}\right)} \beta s \end{cases} \quad \text{if} \quad w = w_{max} \text{ and } \dot{w} \geqslant 0 \tag{2}$$

$$\begin{cases} \sigma_n = \frac{\partial \varphi}{\partial \delta} = \frac{\sigma_f}{w_c} e^{\left(1-\frac{w_{max}}{w_c}\right)} \delta \\ \tau_s = \frac{\partial \varphi}{\partial s} = \frac{\tau_f}{w_c} e^{\left(1-\frac{w_{max}}{w_c}\right)} \beta s \end{cases} \quad \text{if} \quad w < w_{max} \text{ or } \dot{w} < 0 \tag{3}$$

where e is the Neper constant, σ_f is the maximum cohesive normal traction and w_c is a characteristic opening displacement.

The area enclosed by cohesive curves for mode-I and mode-II is the same and represents the fracture energy Γ_F.

Whereas mode-I resistance σ_f and mode-II resistance τ_f, the fracture energy can be defined as follows:

$$\Gamma_F^I = \Gamma_F^{II} = \Gamma_F, \quad \begin{cases} \Gamma_F^I = e\sigma_f w_c \\ \Gamma_F^{II} = e\tau_f w_f \end{cases} \tag{4}$$

where: $\tau_f = \beta\sigma_f$ and $w_f = w_c/\beta$.

Therefore, the adopted cohesive law is characterized by three independent parameters: σ_f, τ_f and Γ_F.

4.2. Calibration of the numerical models: the τ_f and Γ_F parameters

The 2D numerical simulations were obtained adopting parameters τ_f and Γ_F as suggested in the Italian recommendation [22].

According to [22], the specific fracture energy Γ_F and the interface shear strength τ_f can be evaluated as:

$$\begin{cases} \Gamma_F = k_g k_b \sqrt{f_{cm} f_{ctm}} \\ \tau_f = 2\Gamma_F / s_u \end{cases} \tag{5}$$

being s_u the maximum interface slip assumed equal to 0.25 mm; k_g is an empirical coefficient (with a mean value assumed equal to 0.077 mm in the case of an in situ impregnation) and k_b is a non-dimensional geometrical coefficient, assumed according to [22] as:

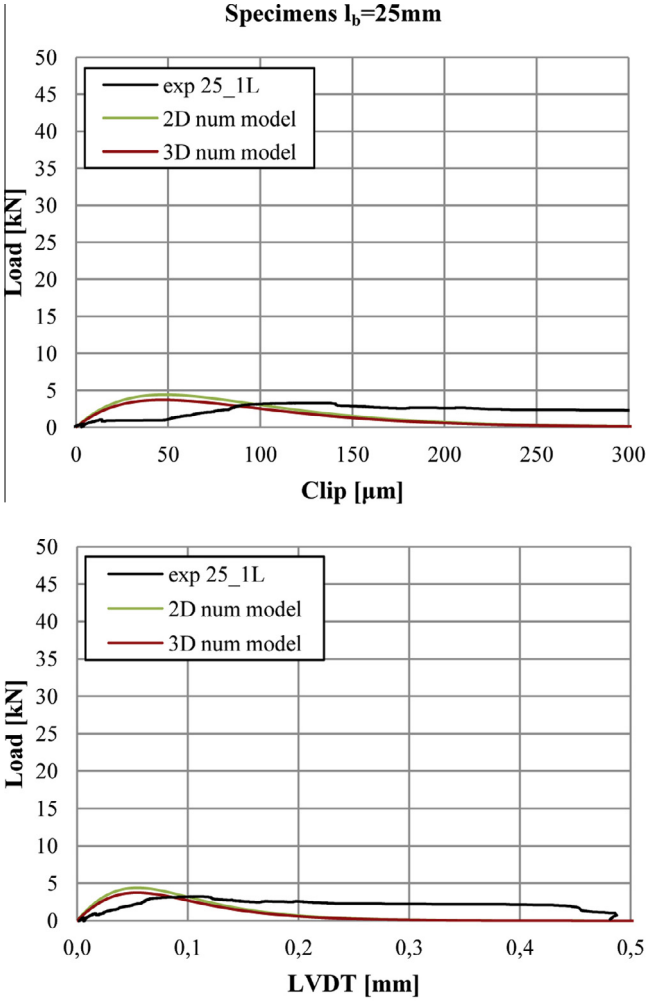

Fig. 11. Comparison between experimental and numerical results, 25 mm bond length.

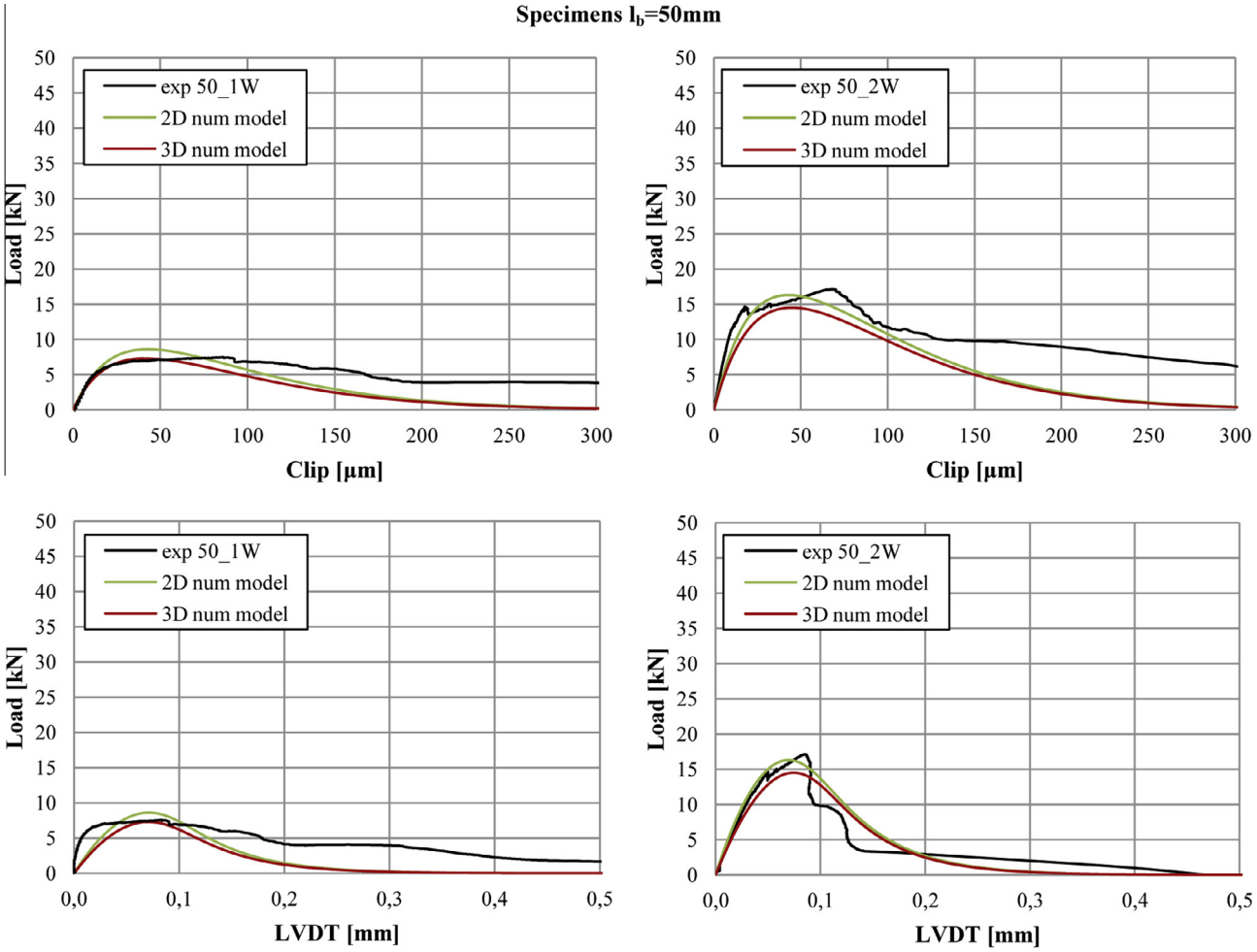

Fig. 12. Comparison between experimental and numerical results, 50 mm bond length.

$$\begin{cases} k_b = \sqrt{\frac{2-b_f/b}{1+b_f/b}} \geqslant 1 & \text{if} \quad b_f/b \geqslant 0.25 \\ k_b = \sqrt{\frac{2-0.25}{1+0.25}} & \text{if} \quad b_f/b < 0.25 \end{cases} \tag{6}$$

The 3D numerical simulations were obtained considering the coefficient k_b equal to 1.

5. Comparison between numerical and experimental results: some observations

The results of the 2D and 3D numerical simulations were analyzed and compared to the experimental ones, in terms of applied force versus LVDT and clip displacement curves (Figs. 11–15 for 25 mm, 50 mm, 100 mm, 150 mm and 200 mm bond lengths, respectively). Since the load–stroke displacement curves were affected by the deformability of the testing system and imperfections of the loading system, these results were not considered in the comparison. Neglecting the data related to a bond length equal to 25 mm, that is too short, both the 2D and 3D numerical simulations were able to catch the experimental curves. In particular, as it is possible to observe from the load–LVDT displacement diagrams, the implemented models were able to follow also the snap-back softening branch of the curve and this allowed to compare the experimental and numerical results both in pre and post-peak phases. The 2D and 3D numerical results are very similar but, generally, the latter show a slightly lower peak load.

The 3D analyses reveals that during the loading process, on the bonded region not only shear stresses parallel to the direction of the applied load, τ_{xy}, in the following defined as τ_L, but also shear stresses in the orthogonal direction, τ_{yz} or simply τ_T, develop (Fig. 16). These are due to the mismatch of the mechanical properties of concrete and FRP that produces a confinement effect in the transversal direction on the concrete substrate. Fig. 17a shows the width effect on the development and distribution of both τ_L and τ_T along the transfer zone. The stress field in three models with different widths (25 mm, 50 mm, 100 mm) and constant bond length (100 mm) was compared at different load levels of the process. It is significant to observe that on the concrete surface:

- Shear stresses τ_L are almost equally distributed along the width and their values remain more or less constant by increasing width.
- Shear stresses τ_T are linearly distributed along the width, with a skew symmetric trend: the maximum positive and negative values occur at the longitudinal boundaries of the bonded region. In addition, these stresses increase with increasing width: this means that the wider the reinforcement width, the more significant the effect of the τ_T is. Fig. 17a shows that, at the peak load level, the values of the τ_T at the edges of the bonded region are approximately 5% of τ_L and 45% of τ_L considering specimens with 25 mm and 100 mm bond length, respectively. This means that a four times increase of the reinforcement width produces a nine times increase of the maximum value of τ_T.

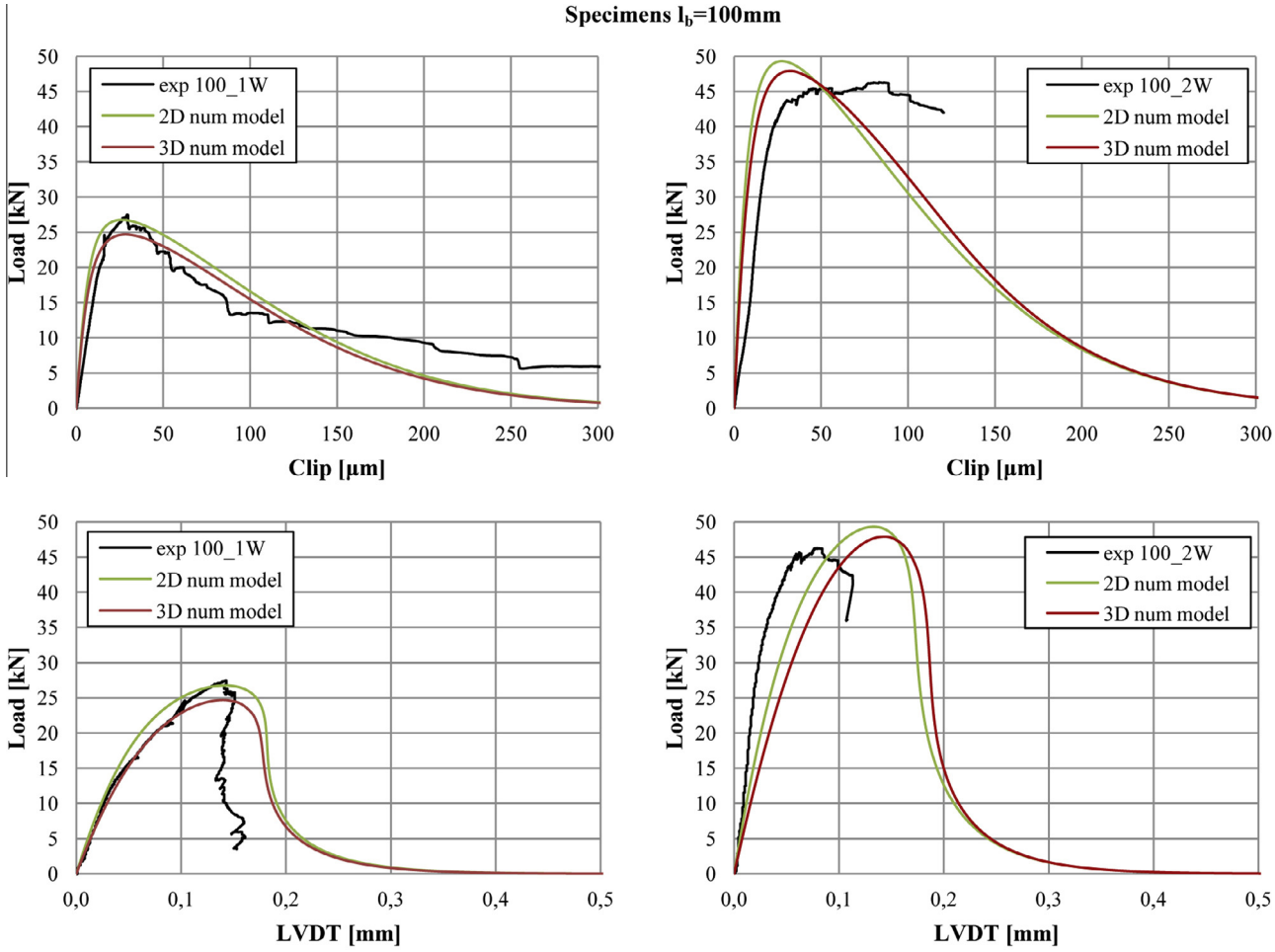

Fig. 13. Comparison between experimental and numerical results, 100 mm bond length.

In addition, Fig. 17b shows the distribution of τ_L and τ_T in a deeper region of concrete (about 1 cm from surface). The shear stresses τ_L are bigger in the central part and their maximum values increase by increasing the reinforcement width. Also the shear stress τ_T are significant compared to the shear stresses τ_L.

Therefore, the 3D analyses show a region of concrete under the transfer load area subjected to a biaxial compression stress field due the superposition of (see, Fig. 18):

i A compression state along transversal direction of the FRP axis, related to the confinement effect produced by not negligible shear stresses τ_T.
ii A compression state along longitudinal direction, related to the particular test arrangement (push–pull setup) considered and described in Section 2.2.

This biaxial compression stress field, more and more significant with increasing width of reinforcement, can affect both the progressive damage and fracture process and, in particular, the ultimate tensile force that can be resisted by the FRP plate before the FRP debonding. As reported in Section 3, the failure in FRP strengthened concrete specimens occurs generally at few millimeters from the concrete-to-adhesive surface, sometimes with the formation of a resistant bulb. Indeed, the debonding process is characterized by the competition of the two damage mechanisms, i.e. the debonding along the interface (mode-II) and the mixed-mode fracture starting at the free end and leading to the formation of the bulb.

A simple mode II damage mechanism is usually expected to occur for the propagation of debonding along the transfer zone. However, the more complex stress field arising in the concrete in view of the confinement effect above described, induces a mixed-mode damage mechanism, which, for the considered experimental setup, may cause higher failure loads. The fracture propagation induced by the described stress field also explains a more dissipative behavior of the 3D model that shows slightly smaller peak loads. Experimentally, it has been observed that the bulb is characterized by a spherical section, whose dimensions are proportional to the reinforcement width. It can be interesting to observe that also the spherical section, that is defined by a double curvature surface, is a consequence of a tri-dimensional stress field in concrete.

However, even if the 3D numerical analyses performed with the model described in Section 4 are able to well simulate the overall loading process, they are not able to capture some important features emerged in the experimental tests. In particular, in the numerical simulations:

1. There is no evidence of any stress or strain concentration suggesting the formation of the bulb at the end of the reinforcement.
2. The failure load to width ratio does not increase with increasing width of the reinforcement, as the confinement effect above introduced and the formation of a resistant bulb related to an increase of the maximum load might suggest.

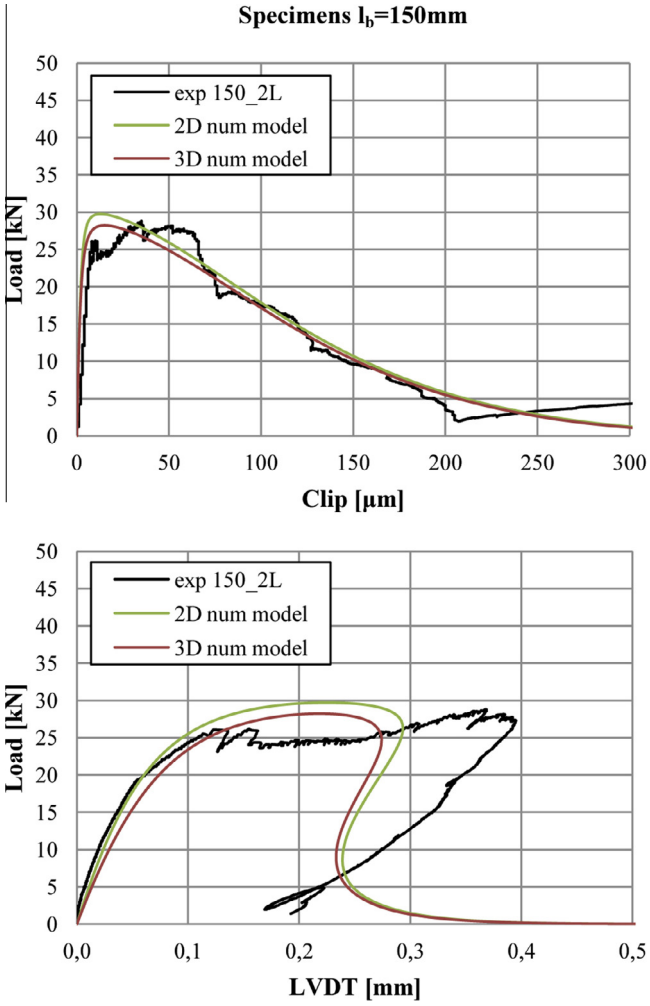

Fig. 14. Comparison between experimental and numerical results, 150 mm bond length.

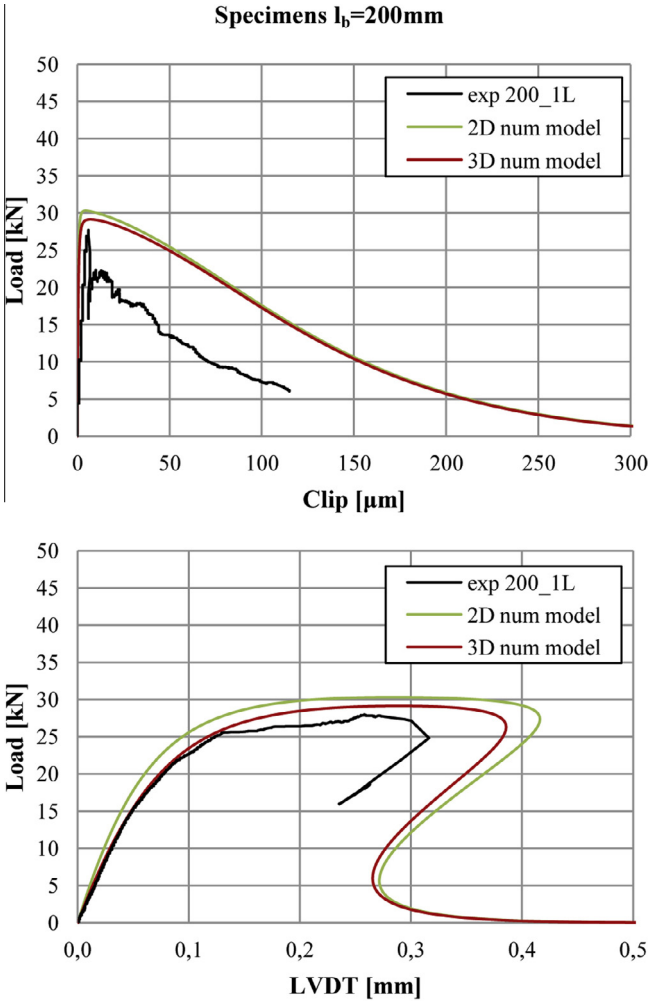

Fig. 15. Comparison between experimental and numerical results, 200 mm bond length.

Fig. 19 shows the effect of the FRP width on the failure load, considering bonded lengths smaller (l_b = 100 mm) or greater (l_b = 200 mm) than the minimum bond length l_e defined according to [22] as follows:

$$l_e = \frac{1}{\tau_f}\sqrt{\frac{\pi^2 E_f t_f \Gamma_f}{2}} \tag{7}$$

Both according to the numerical simulations and to the CNR guidelines [22], the ratio between the failure load and the FRP width decreases to become constant at a certain value with increasing b_f. It is considered that according to the [22] the failure load F_{max} is equal to:

$$\begin{cases} F_{max} = b_f\sqrt{2E_f t_f \Gamma_f} & \text{if} \quad l_b \geqslant l_e \\ F_{max,rid} = F_{max}\frac{l_b}{l_e}\left(2 - \frac{l_b}{l_e}\right) & \text{if} \quad l_b < l_e \end{cases} \tag{8}$$

Therefore, it is possible to assert that both two-dimensional analyses and three-dimensional analyses endowed with linear elastic material models seem not to be completely adequate to explain the experimental observations and some suggestions arisen from them.

6. Numerical modeling with non-linear properties in materials

A different constitutive model was then considered assuming for the concrete a damage-plasticity material model (CDP) [37]. This model is suitable for modeling distinct tensile and compressive strength and assumes that the two main failure mechanisms are tensile cracking and compressive crushing.

The strength domain is a Drucker Prager DP surface modified with an ad-hoc K_c parameter, which distorts the DP surface in the deviatoric plane from a circle to a surface more similar to a Mohr–Coulomb one. K_c physically represents the ratio between distance from the hydrostatic axis of the maximum compression and tension respectively. In the simulation K_c has been kept equal to 2/3, to well approximate a Mohr–Coulomb failure criterion.

A regularization of the tensile corner is also adopted in the model, approximating in the p–q plane the line representing the DP domain with a hyperbola. Regularization is practically obtained in the model with a further correction parameter, referred to as eccentricity, expressing the rate at which the plastic flow potential approaches the linear Drucker–Prager function at high confining pressure stress. The 0.1 default value was assumed.

Dilatance angle ψ of the elasto-plastic part of the inelastic deformation has been kept equal to 25°.

A value equal to 1.16 describing the ratio between the biaxial and mono-axial compression strength has been adopted.

The uniaxial inelastic behavior is expressed with a multi-linear softening model in both tension and compression with strains depurated from the elastic part (Fig. 20). The values adopted in the model are summarized in Table 3.

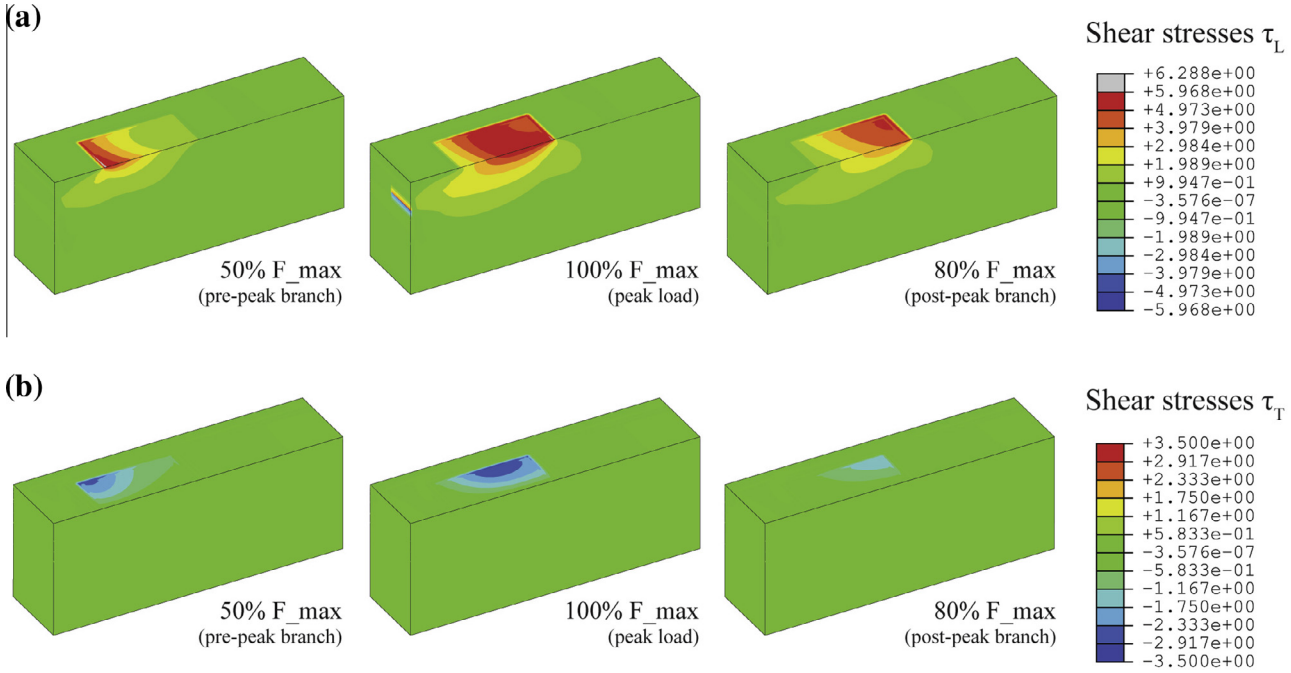

Fig. 16. Shear stresses distribution τ_L (a) and τ_T (b) in the support for different load levels, 100 mm bond length 100 mm width. FRP strip is not visualized.

No interface law was considered, the layer of epoxy resin was modeled and a perfect adhesion between all materials was assumed.

Geometry, constraints and loading conditions were selected to simulate the pull–push configuration as described in Section 4. The discretization was performed adopting both 8-node linear bricks in the regions, near the area involved in the debonding process, and 4-node linear tetrahedron, far from that area in order to reduce the number of degrees of freedom of the numerical model (Fig. 21).

Implicit dynamic procedure was adopted in order to avoid convergence issues.

7. Comparison between numerical and experimental results: new remarks

Inspired by Test# 100_1W and Test# 100_2W, which clearly showed the formation of the resistant bulb, models with a constant reinforcement bond length equal to 100 mm and different widths (from 25 mm to 150 mm) were analyzed and compared.

The results of the numerical analyses are drawn below:

1. The development of damage (Fig. 22) reveals the superposition of two effects which affect both the debonding load and the failure mechanisms, as observed experimentally:
   - i A confinement effect in a concrete volume close to the bonded surface, due to not negligible shear stresses τ_T produced by the mismatch of the mechanical properties of concrete and FRP.
   - ii A diffusive effect, not emerged in the analyses reported in Section 5, that means that the stressed region involved in the debonding process also involved a part of concrete near the bounded region.

   Also the formation of a resistant bulb is detected with the adopted models. Fig. 23 shows the comparison in terms of equivalent plastic strain between the models with 50 mm, 100 mm and 150 mm widths. It is possible to observe that more the width increases, more the strains are confined at the end of the reinforcement, but, when FRP width is equal to concrete width the formation of the bulb is less evident.
2. The ability to identify the interaction of the confinement effect and the diffusive effect and the formation of a resistant bulb, all related to the non-linear behavior of concrete, has enabled to catch the actual effect of the FRP width on strength of the system, defined in terms of ratio between the maximum load and the width of the reinforcement. As it is possible to observe in Fig. 24a with a constant width of the concrete, three different cases can occur:
   - For small values of $\frac{b_f}{b}$ (approximately up to 0.40, for a concrete specimen with the geometrical and mechanical features described in Section 2.1), the ratio between the failure load and the reinforcement width tends to decrease, confirming some suggested predictions, e.g. [22,23]. Indeed if the ratio between the FRP width and the substrate width is too small, the superposition of the confinement effect and diffusive effect is not sufficient to determine on concrete under the transfer load region a significant biaxial compression stress field that could affect the joint strength.
   - For intermediate values of $\frac{b_f}{b}$ (approximately in the range 0.40–0.83, for a concrete specimen with the geometrical and mechanical features described in Section 2.1), the ratio between the failure load and the reinforcement width tends to increase, retracting the suggested predictions, e.g. [22,23]. When the ratio between the FRP and substrate width is large enough, the combination of the confinement effect and diffusive effect determine on concrete under the transfer load region a biaxial compression stress field (more and more relevant by increasing the FRP width) that cause an increase in the joint strength.
   - For large values of $\frac{b_f}{b}$ (approximately greater than 0.83, for a concrete specimen with the geometrical and mechanical features described in Section 2.1) the ratio between the failure load and the reinforcement width tends to decrease. When

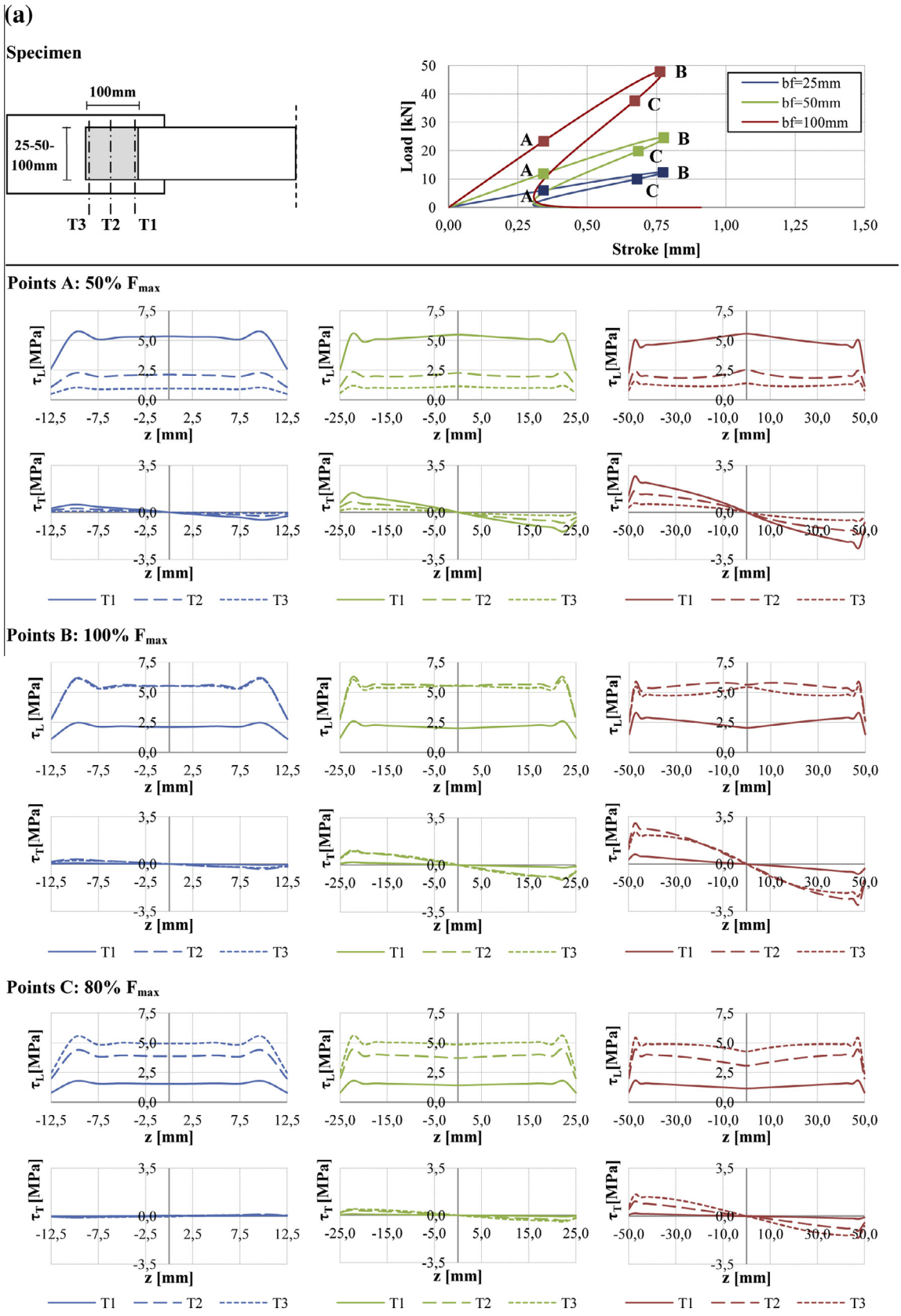

Fig. 17. Distribution of τ_L and τ_T (a) on concrete surface in the interface area; (b) in concrete, at 1 cm from surface.

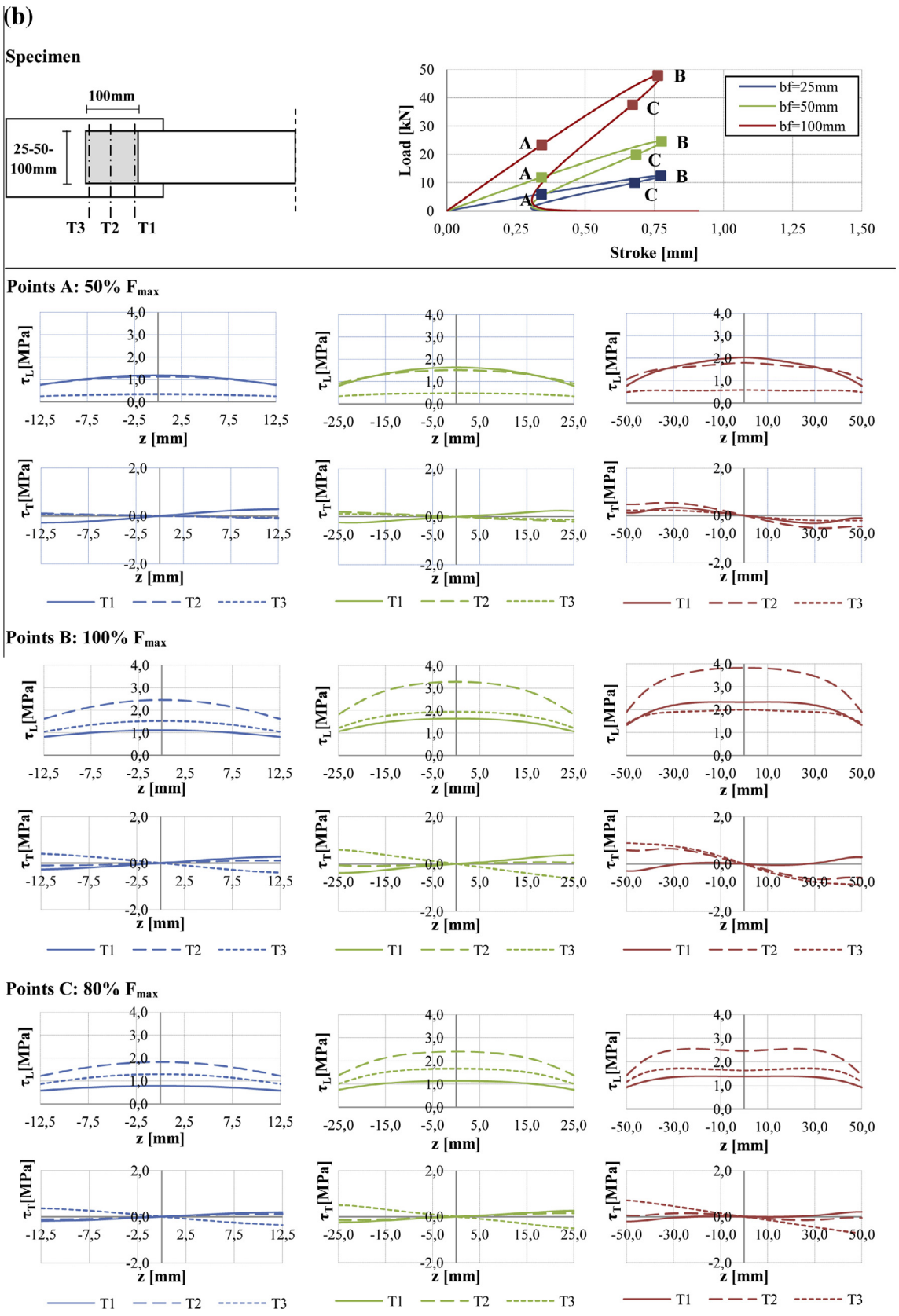

Fig. 17 (*continued*)

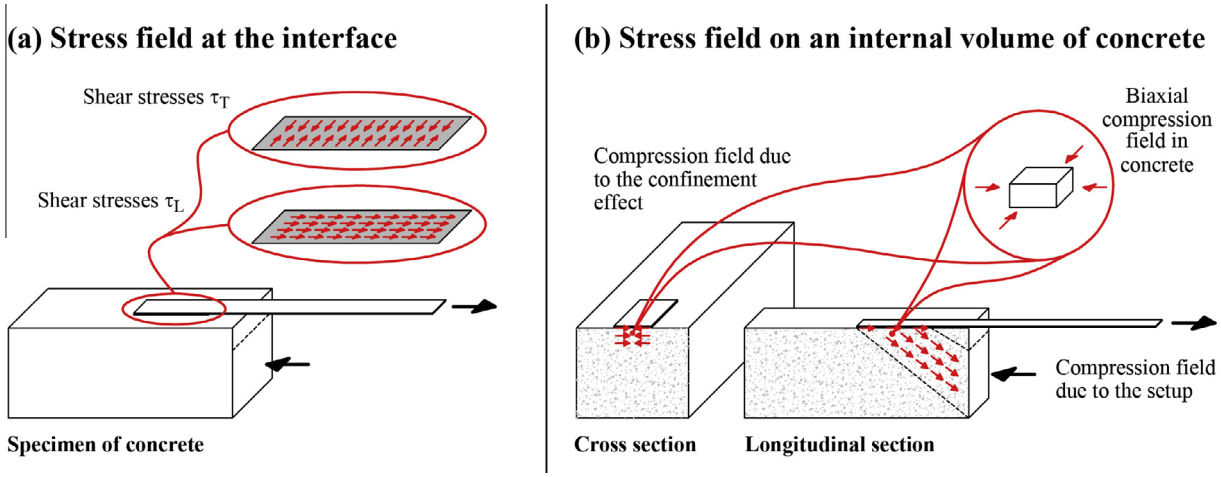

Fig. 18. Illustrative stress field in concrete.

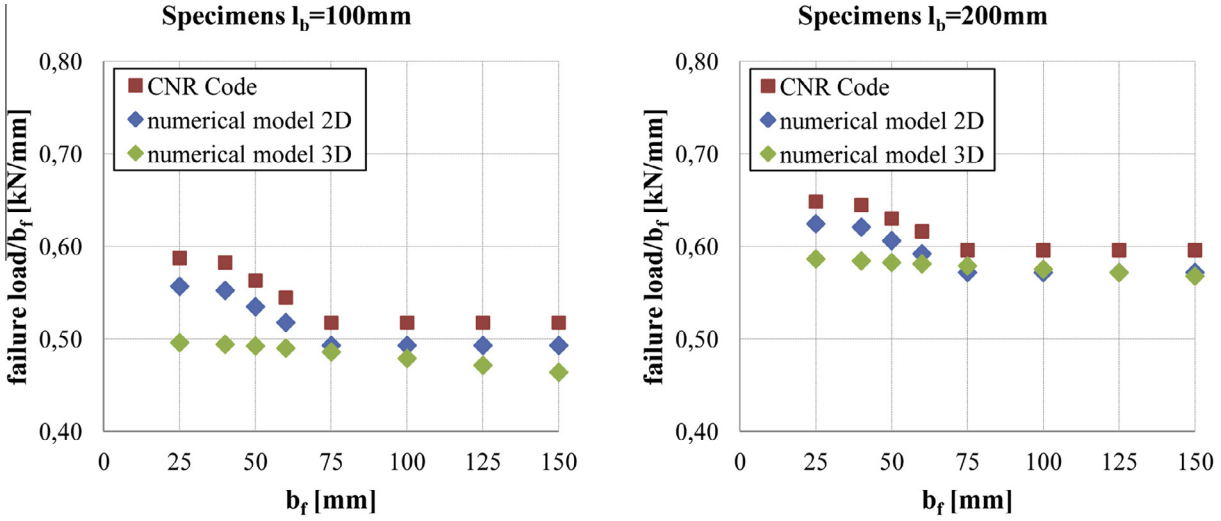

Fig. 19. Relation between the failure load to FRP width ratio and FRP width according to CNR recommendation and the 2D and 3D numerical simulations.

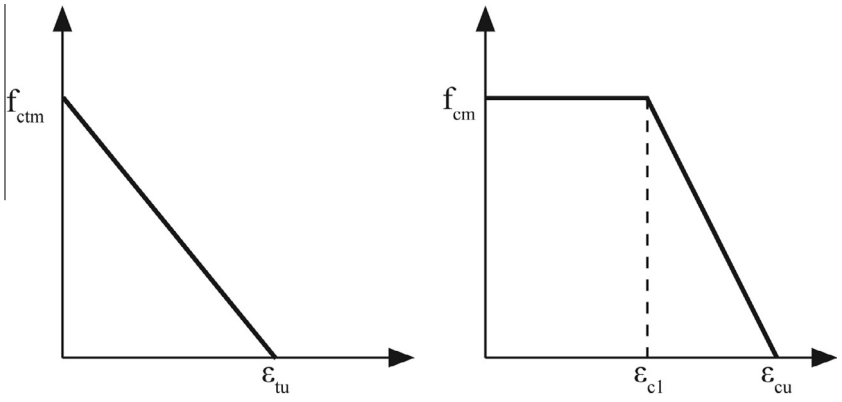

Fig. 20. Stress strain behavior in the post failure regime: tensile behavior (a) and compressive behavior (b).

Table 3
Concrete properties adopted in the analysis.

Mat.	f_{ctm}	ε_{tu}	f_{cm}	ε_{c1}	ε_{cu}
Concrete	2.88	0.0035	32.59	0.0025	0.0035

the FRP width is comparable to the concrete width, the diffusive effect and the confinement effect are not sufficient, for obvious boundary conditions reasons, to determine a further increase of the joint strength.

The experimental program presented in this paper is not exhaustive and it does not allow to show a real and clear trend of the joint strength compared to the FRP width. In Appendix is collected a database with the results obtained by other Authors that tested CFRP sheets on concrete support using a pull–push single shear configuration. The symbol (*) marks the tests where the effect of the width was investigated. As it is possible to see, the results are conflicting and it is not possible to bring out a clear trend of the joint strength compared to the FRP width. The difficulties in comparing these results could be due to several aspects. Surely

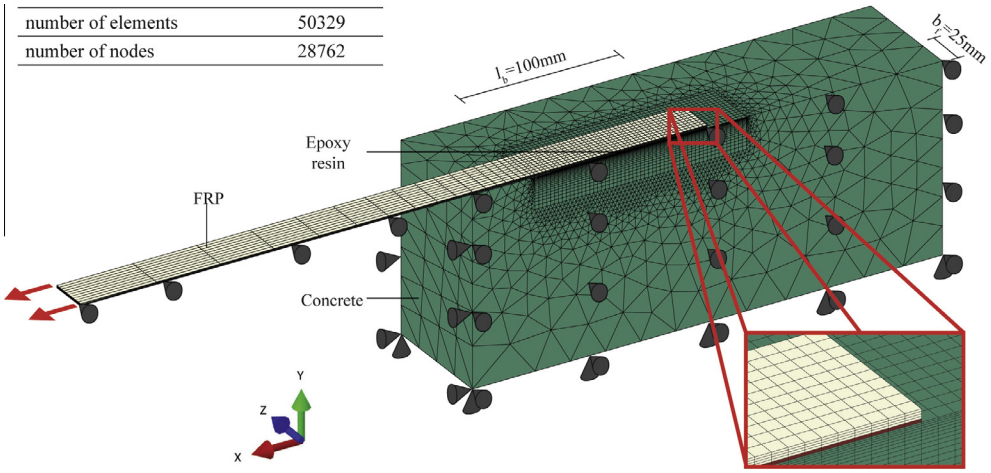

Fig. 21. Geometry, constraints, loading conditions and discretization of the 3D numerical model with 100 mm bond length and 50 mm FRP width.

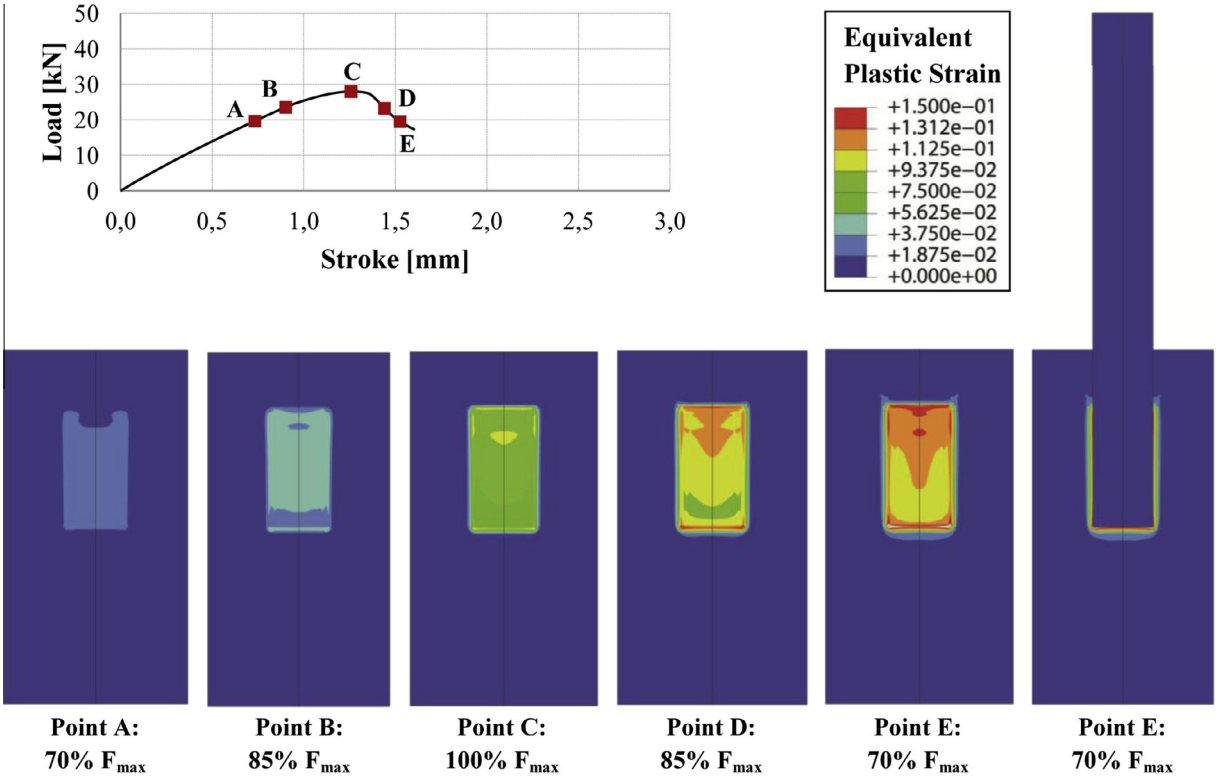

Fig. 22. Equivalent plastic strains distribution.

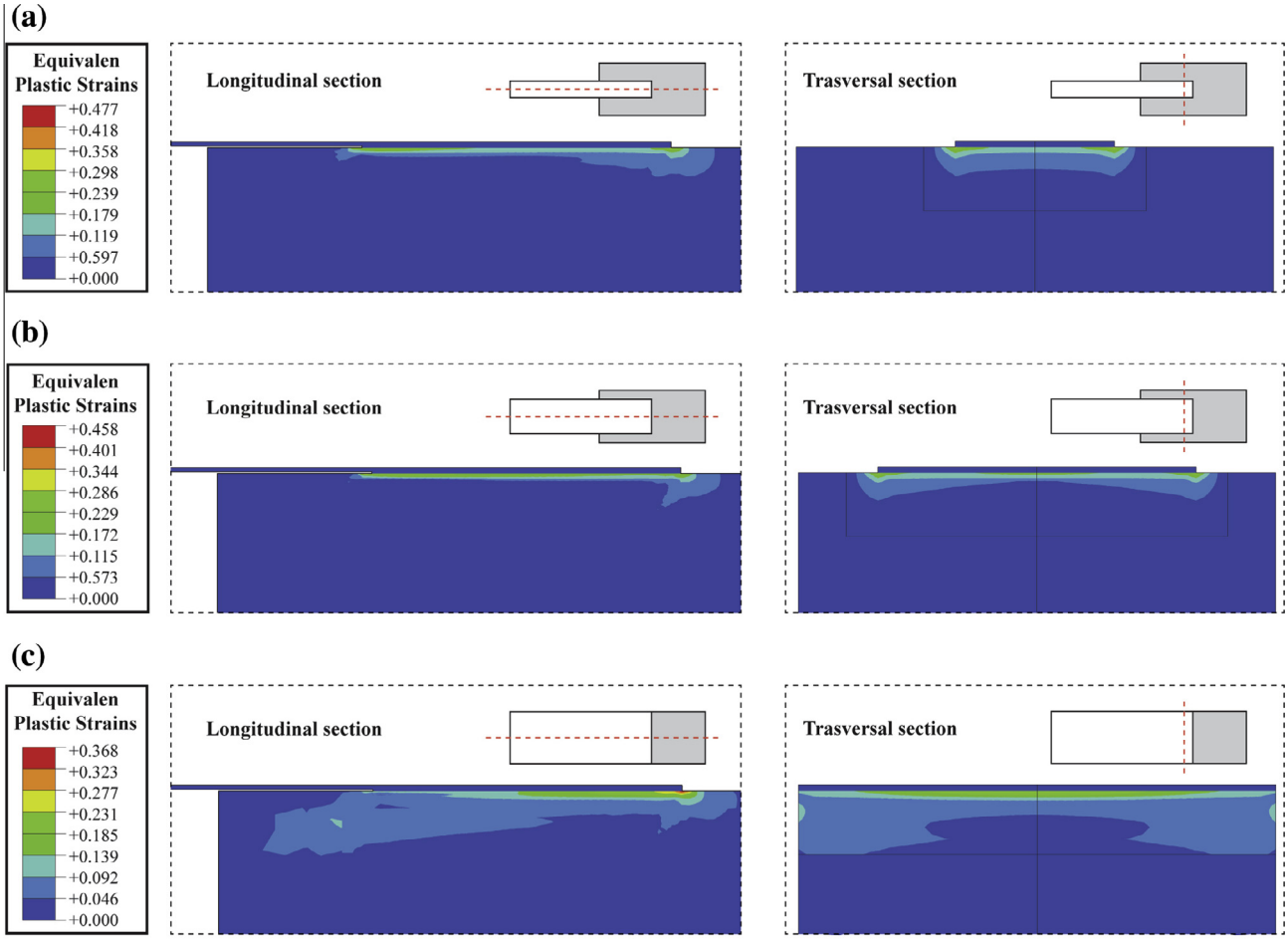

Fig. 23. Comparison between 100 mm bond length and 50 mm (a), 100 mm (b), 150 mm (c) FRP width in terms of equivalent plastic strains.

the way used to perform the tests has affected the reliability of the results: in particular the choice of the feedback signal that determine the possibility to capture the second peak and the formation of the bulb. Then the difference in the thickness of the reinforcement, concrete resistance, dimension of the specimen have surely played an important role on the strength of the joint.

However, accordingly to the numerical findings shown in Fig. 24a, other Authors observed the same trend of the failure load with respect to the FRP width to concrete width ratio, Fig. 24b. In particular, in [27] an increasing trend was experimentally detected for specimens with $\frac{b_f}{b} < 0.50$. The contrast of this result with the predictions of empirical equations proposed, e.g. in [22,23], was also highlighted in [27]. The curve experimentally obtained by [28] is quite similar to the one obtained by numerical simulation in Fig 24a. A decrease, an increase and a final decrease of the load-carrying capacity with an increase of the FRP width was observed for specimens with $\frac{b_f}{b}$ in a range between 0.17 and 0.67: this in accordance with what discussed above on the role played by confinement and diffusive effects. In addition, it can be observed that the possibility to grab the formation of the resistant bulb – more and more relevant by increasing the width of reinforcement – may explain why, respect what detected in [28], the Authors found the maximum value of the load-carrying capacity to be in correspondence of higher value of the FRP width to concrete width ratio. At last, the results obtained by Ren and reported in [18] are rather heterogeneous: they clearly show how the concrete and FRP properties can affect the strength of the whole system. It has to be observed that in this case, a comparison between the experimental results and the Code provision was not possible due to the lack of data concerning the dimension of the specimen.

3. As shown by several Authors, different experimental setups can been used for pull-out test to determine the FRP-to-concrete bond strength [7]. Fig. 25 shows a comparison in terms of strength of FRP-to-concrete bonded joint considering two different single pull-out shear test configurations: a push–pull and a pull–pull. Considering the same size specimen, the failure load obtained numerically by a pull–pull configuration is significantly lower than the failure load obtained by a pull–push one. As it is well known, different boundary conditions produce different stress transmission in concrete, that means significant differences in the strength and the post failure response of the joint. For this reason, the results and considerations coming from different experimental setups of pull-out tests cannot be compared. The reinforcement design of a real structure cannot disregard these considerations. For instance, the strengthening and stiffening of the bottom side of a simply supported beam can be design referring to a push–pull test configuration. In this situation, the reinforced beam is characterized by a stress distribution that can be consider similar to the one shown in

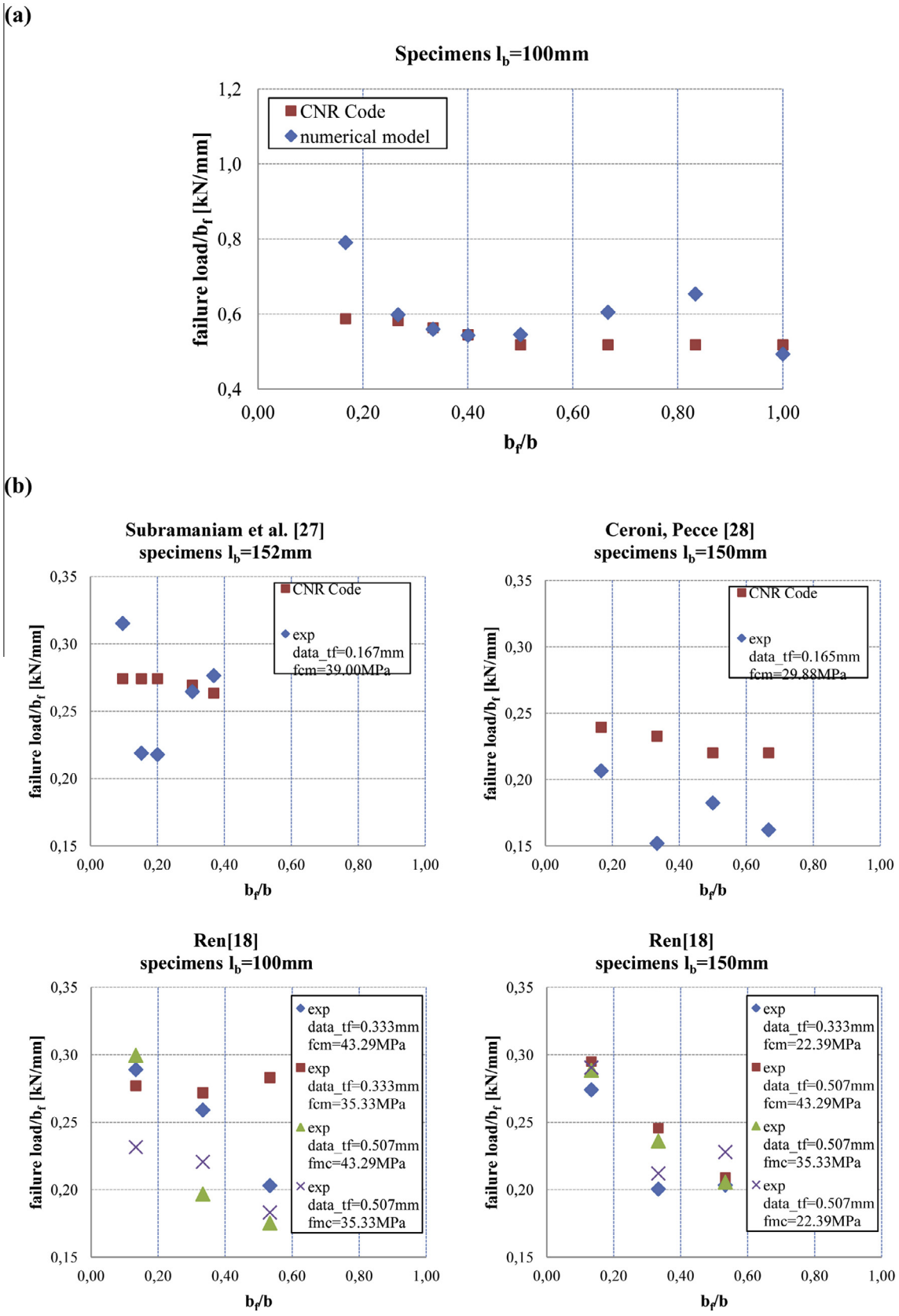

Fig. 24. Relation between the failure load to FRP width ratio and FRP width to concrete width according to Italian CNR recommendation and the numerical simulations (a), experimental results collected in literature (b).

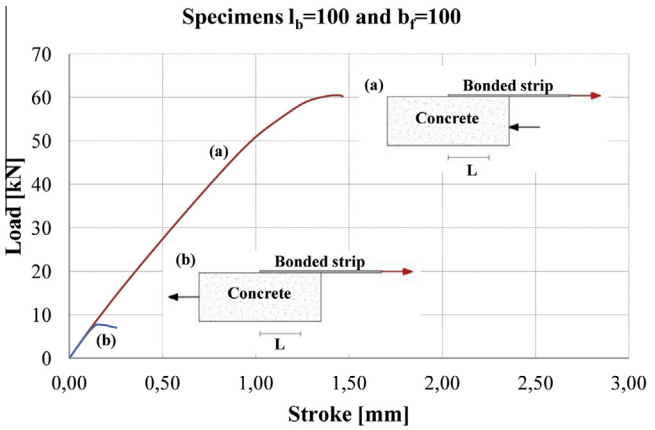

Fig. 25. Comparison the joint strength in two different setups: pull–push shear test configuration (a), pull–pull shear test configuration (b).

Fig. 18 where the reinforcement is bonded in the tensile side of the member. Whereas, the stress field that emerges in a FRP reinforced cantilever beam can be analyzed referring to a pull–pull setup.

8. Conclusions

In this paper, the entire debonding process between FRP strips and concrete substrate was examined and the influence of the geometric variables, in particular the width of the reinforcement, on the joint strength was investigated.

Experiments based on single lap shear test were conducted and the complete failure process was monitored using a clip gage located at the free end of the plate as the feedback signal to the servo-controller. The creation of a bulb in the concrete at the end of the reinforcement turned out to have a non-negligible influence on the maximum load which can be transmitted by the joint.

Numerical analyses by means of 2D and 3D FE models were performed to interpreter and better comprehend the debonding phenomena experimentally observed. Two different approaches were investigated: (a) a numerical model based on elastic and linear materials with the non-linearities concentrated at the interface (b) a numerical model, based on a non-linear constitutive model for concrete and a perfect adhesion between all the materials.

The following conclusions can be drawn:

1. The debonding phenomena between FRP strips and concrete substrate is a tri-dimensional problem, characterized by a complex tri-dimensional stress field, therefore 2D numerical analyses do not seem completely adequate to explain the experimental evidences.
2. Simplified numerical models based on linear materials and non-linear interface, i.e. approach (a), can simulate the system response in terms of applied forces versus displacement curves. However, these models are able to describe only a mode II debonding along the interface and they are totally unable to describe a mix-mode failure involving also the substrate. Only 3D numerical models with a non-linear constitutive model for concrete, i.e. approach (b), are suitable to correctly mimic the debonding process in terms of damage development and joint strength.
3. The development of damage due to the debonding process reveals the superposition of a confinement effect, in a concrete volume close to the bonded surface, and a diffusive effect, in a part of concrete near the bonded regions. These two effects influence both the debonding load and the failure mechanisms, with the formation of the resistant bulb.
4. The relative width of FRP and concrete strongly affects the strength of the system. In particular: (i) with small values of $\frac{b_f}{b}$, the relative joint strength tends to decrease; (ii) with intermediate values of $\frac{b_f}{b}$, the relative joint strength tends to increase; (iii) with large values of $\frac{b_f}{b}$, the relative joint strength tends to decrease. Preliminary numerical investigations seem to show that the size effect plays an important role on the definition of the above-mentioned range of $\frac{b_f}{b}$. However additional experimental and numerical work should be done to clarify this problem.
5. The transmission of forces within the specimens is strongly affected by the boundary conditions which cause very different stress fields in the substrate. Regression analyses of experimental data obtained by different test configurations must be performed carefully. Then, this has to be taken into consideration in the design of the reinforcement for different structures.

Future developments on the observed phenomena can concern experimental and numerical investigations aimed to study:

1. The scaling effect, that means the analysis of concrete specimens with different geometrical dimensions, in order to consider also the response of reinforced systems equivalent to real practical applications.
2. The influence of both the confinement effect and the diffusive effect in the debonding process, on varying of both reinforcement and concrete widths. This can be useful in order to analyze the possible interaction of two or more parallel reinforcing FRP strips in order to optimize their mechanical performance.
3. A systematic comparison between the results of different configurations of pull-out tests deepening what suggested in Section 7, point 3. This means to analyze the different stress fields due to the use of different test setup and explain how they can determine very different joint strengths.

Acknowledgments

GB gratefully acknowledges the Unesco Chair of the Politecnico di Milano – Mantova Campus for providing support for her graduate studies.

The authors would also like to thank Mapei Spa, that provided materials and assistance for the experiments, and the technical staff of the structures laboratory at Politecnico di Milano, particularly Paolo Broglia and Antonio Cocco, for their assistance during the experimental work.

Appendix

The table reports a complete database of the experimental results from several Authors that tested CFRP sheets on concrete support using a push–pull single shear configuration. Unfortunately some data are lacking of information regarding the dimensions of the concrete prism. The symbols (*) and (**) mark the tests were the width effect and the bond length effect are analyzed, respectively. It has to be added that the parameter h_c is related to the hight of the concrete free edge (=height of concrete prism, h, – height of the supported block) (see Appendix).

Appendix

Database of the experimental results for single shear tests setup.

Authors	Specimen #	FRP					Concrete prism					Load		
		t_f [mm]	b_f [mm]	l_b [mm]	E_f [GPa]	f_f [MPa]	b [mm]	l [mm]	h [mm]	h_c [mm]	f_{cm} [MPa]	F_{max} [kN]	b_f/b	F/b_f
Takeo et al. [18]	**1-11	0.167	40	100	230	3481	100	–	–	–	28.52	8.75		
	**1-21	0.167	40	200	230	3481	100	–	–	–	28.52	9.30		
	**1-31	0.167	40	300	230	3481	100	–	–	–	28.52	9.30		
	**1-41	0.167	40	500	230	3481	100	–	–	–	28.52	8.05		
	**1-42	0.167	40	500	230	3481	100	–	–	–	28.52	8.05		
	**1-12	0.167	40	100	230	3481	100	–	–	–	26.33	8.85		
	**1-22	0.167	40	200	230	3481	100	–	–	–	26.33	8.50		
	**1-32	0.167	40	300	230	3481	100	–	–	–	26.33	8.30		
	**1-51	0.167	40	500	230	3481	100	–	–	–	26.13	8.45		
	**1-52	0.167	40	500	230	3481	100	–	–	–	26.13	7.30		
	2-11	0.167	40	100	230	3481	100	–	–	–	24.67	8.75		
	2-12	0.167	40	100	230	3481	100	–	–	–	24.67	8.85		
	2-13	0.167	40	100	230	3481	100	–	–	–	25.84	7.75		
	2-14	0.167	40	100	230	3481	100	–	–	–	25.84	7.65		
	2-15	0.167	40	100	230	3481	100	–	–	–	24.09	9.00		
	2-21	0.334	40	100	230	3481	100	–	–	–	24.67	12.00		
	2-22	0.334	40	100	230	3481	100	–	–	–	24.67	10.80		
	2-31	0.501	40	100	230	3481	100	–	–	–	24.67	12.65		
	2-32	0.501	40	100	230	3481	100	–	–	–	24.67	14.35		
	2-41	0.165	40	100	373	2942	100	–	–	–	24.09	11.55		
	2-42	0.165	40	100	373	2942	100	–	–	–	24.09	11.00		
	2-51	0.167	40	100	230	3481	100	–	–	–	25.84	9.85		
	2-52	0.167	40	100	230	3481	100	–	–	–	25.84	9.50		
	2-61	0.167	40	100	230	3481	100	–	–	–	25.84	8.80		
	2-62	0.167	40	100	230	3481	100	–	–	–	25.84	9.25		
	2-71	0.167	40	100	230	3481	100	–	–	–	25.84	7.65		
	2-72	0.167	40	100	230	3481	100	–	–	–	25.84	6.80		
	2-81	0.167	40	100	230	3481	100	–	–	–	49.34	7.75		
	2-82	0.167	40	100	230	3481	100	–	–	–	49.34	8.05		
	2-91	0.167	40	100	230	3481	100	–	–	–	24.09	6.75		
	2-92	0.167	40	100	230	3481	100	–	–	–	24.09	6.80		
	2-101	0.111	40	100	230	3481	100	–	–	–	24.67	7.70		
	2-102	0.111	40	100	230	3481	100	–	–	–	24.67	6.95		
Bizindavyi [44]	BN25	0.330	25.4	160	75.7	1014	150	400	150	0	35.28	8.50		
	BN32	0.660	25.4	320	75.7	1014	150	400	150	0	35.28	15.10		
Ueda et al. [18]	Ueda_B1	0.11	100	200	230	3479	500	–	–	–	24.70	20.60		
	Ueda_B2	0.33	100	200	230	3479	500	–	–	–	40.90	38.00		
	Ueda_B3	0.33	100	200	230	3479	500	–	–	–	45.90	34.10		
Zhao et al. [18]	**NJ2	0.083	100	100	240	3550	150	–	–	–	15.99	11.00		
	**NJ3	0.083	100	150	240	3550	150	–	–	–	15.99	11.25		
	**NJ4	0.083	100	100	240	3550	150	–	–	–	28.63	12.50		
	**NJ5	0.083	100	150	240	3550	150	–	–	–	28.63	12.25		
	**NJ6	0.083	100	150	240	3550	150	–	–	–	28.63	12.75		
Wu et al. [18]	S-CFS-400-25a	0.222	40	250	230	4200	100	–	–	–	57.60	15.40		
	S-CFS-400-25b	0.222	40	250	230	4200	100	–	–	–	57.60	13.90		
	S-CFS-400-25c	0.222	40	250	230	4200	100	–	–	–	57.60	13.00		
	S-CFS-300-25a	0.167	40	250	390	4400	100	–	–	–	57.60	12.00		
	S-CFS-300-25b	0.167	40	250	390	4400	100	–	–	–	57.60	11.90		
	S-CFS-900-25a	0.500	40	250	230	4200	100	–	–	–	57.60	25.90		
	S-CFS-900-25b	0.500	40	250	230	4200	100	–	–	–	57.60	23.40		
	S-CFS-900-25c	0.500	40	250	230	4200	100	–	–	–	57.60	23.70		
Ren [18]	DLUT30-3G	0.507	50	60	83.03	3271	150	–	–	–	35.33	9.42		
	*DLUT30-1C	0.330	20	100	207	3890	150	–	–	–	35.33	5.54	0.133	0.277
	*DLUT30-4C	0.330	50	100	207	3890	150	–	–	–	35.33	11.08	0.333	0.222
	*DLUT30-5C	0.330	50	100	207	3890	150	–	–	–	35.33	16.10	0.333	0.322
	*DLUT30-7C	0.330	80	100	207	3890	150	–	–	–	35.33	22.64	0.533	0.283
	*DLUT50-1C	0.330	20	100	207	3890	150	–	–	–	43.29	5.78	0.133	0.289
	*DLUT50-4C	0.330	50	100	207	3890	150	–	–	–	43.29	12.95	0.333	0.259
	*DLUT50-6C	0.330	50	100	207	3890	150	–	–	–	43.29	16.24	0.333	0.203
	*DLUT30-1G	0.507	20	100	83.03	3271	150	–	–	–	35.33	4.63	0.133	0.232
	*DLUT30-4G	0.507	50	100	83.03	3271	150	–	–	–	35.33	11.03	0.333	0.221
	*DLUT30-7G	0.507	80	100	83.03	3271	150	–	–	–	35.33	14.65	0.533	0.183
	*DLUT50-1G	0.507	20	100	83.03	3271	150	–	–	–	43.29	5.99	0.133	0.300
	*DLUT50-4G	0.507	50	100	83.03	3271	150	–	–	–	43.29	9.84	0.333	0.197
	*DLUT50-6G	0.507	80	100	83.03	3271	150	–	–	–	43.29	14.02	0.533	0.175

(*continued on next page*)

Appendix (*continued*)

Authors	Specimen #	FRP					Concrete prism					Load		
		t_f [mm]	b_f [mm]	l_b [mm]	E_f [GPa]	f_f [MPa]	b [mm]	l [mm]	h [mm]	h_c [mm]	f_{cm} [MPa]	F_{max} [kN]	b_f/b	F/b_f
	*DLUT15-2C	0.330	20	150	207	3890	150	–	–	–	22.39	5.48	0.133	0.274
	*DLUT15-5C	0.330	50	150	207	3890	150	–	–	–	22.39	10.02	0.333	0.200
	*DLUT15-7C	0.330	80	150	207	3890	150	–	–	–	22.39	16.27	0.533	0.203
	*DLUT30-2C	0.330	20	150	207	3890	150	–	–	–	35.33	4.61	0.133	0.231
	*DLUT30-6C	0.330	50	150	207	3890	150	–	–	–	35.33	21.71	0.333	0.434
	*DLUT50-5C	0.330	20	150	207	3890	150	–	–	–	43.29	16.72	0.133	0.334
	*DLUT50-7C	0.330	50	150	207	3890	150	–	–	–	43.29	22.80	0.333	0.285
	*DLUT15-2G	0.507	20	150	83.03	3271	150	–	–	–	22.39	5.81	0.133	0.291
	*DLUT15-5G	0.507	50	150	83.03	3271	150	–	–	–	22.39	10.60	0.333	0.212
	*DLUT15-7G	0.507	80	150	83.03	3271	150	–	–	–	22.39	18.23	0.533	0.228
	*DLUT30-2G	0.507	20	150	83.03	3271	150	–	–	–	35.33	5.77	0.133	0.289
	*DLUT30-6G	0.507	50	150	83.03	3271	150	–	–	–	35.33	11.80	0.333	0.236
	*DLUT30-8G	0.507	80	150	83.03	3271	150	–	–	–	35.33	16.44	0.533	0.206
	*DLUT50-2G	0.507	20	150	83.03	3271	150	–	–	–	43.29	5.90	0.133	0.295
	*DLUT50-5G	0.507	50	150	83.03	3271	150	–	–	–	43.29	12.28	0.333	0.246
	*DLUT50-7G	0.507	80	150	83.03	3271	150	–	–	–	43.29	16.71	0.533	0.209
Yao et al. [7]	**I-1	0.165	25	75	256	4114	150	350	150	5	23.00	4.75		
	**I-2	0.165	25	85	256	4114	150	350	150	5	23.00	5.69		
	**I-3	0.165	25	95	256	4114	150	350	150	5	23.00	5.76		
	**I-4	0.165	25	95	256	4114	150	350	150	5	23.00	5.76		
	**I-5	0.165	25	95	256	4114	150	350	150	5	23.00	6.17		
	**I-6	0.165	25	115	256	4114	150	350	150	5	23.00	5.96		
	**I-7	0.165	25	145	256	4114	150	350	150	5	23.00	5.95		
	**I-8	0.165	25	190	256	4114	150	350	150	5	23.00	6.68		
	**I-9	0.165	25	190	256	4114	150	350	150	5	23.00	6.35		
	**I-10	0.165	25	95	256	4114	150	350	150	75	23.00	6.17		
	**I-11	0.165	25	75	256	4114	150	350	150	120	23.00	5.72		
	**I-12	0.165	25	85	256	4114	150	350	150	120	23.00	6.00		
	**I-13	0.165	25	95	256	4114	150	350	150	120	23.00	6.14		
	**I-14	0.165	25	115	256	4114	150	350	150	120	23.00	6.19		
	**I-15	0.165	25	145	256	4114	150	350	150	120	23.00	6.27		
	**I-16	0.165	25	190	256	4114	150	350	150	120	23.00	7.03		
	**II-1	0.165	25	95	256	4114	150	350	150	120	22.90	5.20		
	**II-2	0.165	25	95	256	4114	150	350	150	120	22.90	6.75		
	**II-3	0.165	25	95	256	4114	150	350	150	120	22.90	5.51		
	**II-4	0.165	25	190	256	4114	150	350	150	120	22.90	7.02		
	**II-5	0.165	25	190	256	4114	150	350	150	120	22.90	7.07		
	**II-6	0.165	25	190	256	4114	150	350	150	120	22.90	6.98		
	*III-1	0.165	25	100	256	4114	150	350	100	120	27.10	5.94	0.167	0.238
	*III-2	0.165	50	100	256	4114	150	350	100	120	27.10	11.66	0.333	0.233
	*III-3	0.165	75	100	256	4114	150	350	100	120	27.10	14.63	0.500	0.195
	*III-4	0.165	100	100	256	4114	150	350	100	120	27.10	19.07	0.667	0.191
	*III-5	0.165	85	100	256	4114	100	350	100	120	27.10	15.08	0.850	0.177
	*III-6	0.165	100	100	256	4114	100	350	100	120	27.10	15.75	1.000	0.158
	IV-1	0.165	25	95	256	4114	150	350	150	5	18.90	5.86		
	IV-2	0.165	25	95	256	4114	150	350	150	5	18.90	5.90		
	IV-3	0.165	25	95	256	4114	150	350	150	5	19.80	5.43		
	IV-4	0.165	25	95	256	4114	150	350	150	5	19.80	5.76		
	IV-5	0.165	25	95	256	4114	150	350	150	15	18.90	5.00		
	IV-6	0.165	25	95	256	4114	150	350	150	15	19.80	7.08		
	IV-7	0.165	25	95	256	4114	150	350	150	30	18.90	5.50		
	IV-8	0.165	25	95	256	4114	150	350	150	30	19.80	5.93		
	IV-9	0.165	25	95	256	4114	150	350	150	45	18.90	5.38		
	IV-10	0.165	25	95	256	4114	150	350	150	45	19.80	6.60		
	IV-11	0.165	25	95	256	4114	150	350	150	60	18.90	5.51		
	IV-12	0.165	25	95	256	4114	150	350	150	60	19.80	5.67		
	IV-13	0.165	25	95	256	4114	150	350	150	90	18.90	6.31		
	IV-14	0.165	25	95	256	4114	150	350	150	90	19.80	6.19		
	*V-1	0.165	15	95	256	4114	150	350	100	60	21.10	3.81	0.100	0.254
	*V-2	0.165	15	95	256	4114	150	350	100	60	21.10	4.41	0.100	0.294
	*V-3	0.165	25	95	256	4114	150	350	100	60	21.10	6.26	0.167	0.250
	*V-4	0.165	50	95	256	4114	150	350	100	60	21.10	12.22	0.333	0.244
	*V-5	0.165	75	95	256	4114	150	350	100	60	21.10	14.29	0.500	0.191
	*V-6	0.165	100	95	256	4114	150	350	100	60	21.10	15.58	0.667	0.156
	V-7	0.165	80	95	256	4114	100	350	100	60	21.10	14.27		
	V-8	0.165	80	95	256	4114	100	350	100	60	21.10	13.78		
	V-9	0.165	90	95	256	4114	100	350	100	30	21.10	13.56		

Appendix (*continued*)

Authors	Specimen #	FRP					Concrete prism					Load		
		t_f [mm]	b_f [mm]	l_b [mm]	E_f [GPa]	f_f [MPa]	b [mm]	l [mm]	h [mm]	h_c [mm]	f_{cm} [MPa]	F_{max} [kN]	b_f/b	F/b_f
	V-10	0.165	90	95	256	4114	100	350	100	5	21.10	15.66		
	V-11	0.165	100	95	256	4114	100	350	100	30	21.10	15.57		
	V-12	0.165	100	95	256	4114	100	350	100	5	21.10	17.43		
	**VI-1	0.165	25	95	256	4114	150	350	150	60	21.90	6.01		
	**VI-2	0.165	25	95	256	4114	150	350	150	60	21.90	5.85		
	**VI-3	0.165	25	145	256	4114	150	350	150	60	21.90	5.76		
	**VI-4	0.165	25	145	256	4114	150	350	150	60	21.90	5.73		
	**VI-5	0.165	25	190	256	4114	150	350	150	60	21.90	5.56		
	**VI-6	0.165	25	190	256	4114	150	350	150	60	21.90	5.58		
	**VI-7	0.165	25	240	256	4114	150	350	150	60	21.90	5.91		
	**VI-8	0.165	25	240	256	4114	150	350	150	60	21.90	5.05		
	**VII-1	0.165	25	95	256	4114	150	350	150	60	24.90	6.80		
	**VII-2	0.165	25	95	256	4114	150	350	150	60	24.90	6.62		
	**VII-3	0.165	25	145	256	4114	150	350	150	60	24.90	7.33		
	**VII-4	0.165	25	145	256	4114	150	350	150	60	24.90	6.49		
	**VII-5	0.165	25	190	256	4114	150	350	150	60	24.90	7.07		
	**VII-6	0.165	25	190	256	4114	150	350	150	60	24.90	7.44		
	**VII-7	0.165	25	240	256	4114	150	350	150	60	24.90	7.16		
	**VII-8	0.165	25	240	256	4114	150	350	150	60	24.90	6.24		
Subramaniam et al. [27]	*W-1	0.167	46	152	230	3830	125	330	125	–	39.00	12.90	0.368	0.280
	*W-2	0.167	46	152	230	3830	125	330	125	–	39.00	12.05	0.368	0.262
	*W-3	0.167	46	152	230	3830	125	330	125	–	39.00	13.20	0.368	0.287
	*W-4	0.167	38	152	230	3830	125	330	125	–	39.00	10.09	0.304	0.266
	*W-5	0.167	38	152	230	3830	125	330	125	–	39.00	10.02	0.304	0.264
	*W-6	0.167	25	152	230	3830	125	330	125	–	39.00	5.54	0.200	0.222
	*W-7	0.167	25	152	230	3830	125	330	125	–	39.00	5.44	0.200	0.218
	*W-8	0.167	25	152	230	3830	125	330	125	–	39.00	5.36	0.200	0.214
	*W-9	0.167	19	152	230	3830	125	330	125	–	39.00	4.27	0.152	0.225
	*W-10	0.167	19	152	230	3830	125	330	125	–	39.00	4.05	0.152	0.213
	*W-11	0.167	12	152	230	3830	125	330	125	–	39.00	3.96	0.096	0.330
	*W-12	0.167	12	152	230	3830	125	330	125	–	39.00	3.89	0.096	0.324
	*W-13	0.167	12	152	230	3830	125	330	125	–	39.00	3.50	0.096	0.292
Toutanji et al. [45]	I-1	0.495	50	100	110	660	200	200	130	–	17.00	7.56		
	I-2	0.660	50	100	110	660	200	200	130	–	17.00	9.29		
	I-3	0.825	50	100	110	660	200	200	130	–	17.00	11.64		
	I-4	0.990	50	100	110	660	200	200	130	–	17.00	12.86		
	II-1	0.495	50	100	110	660	200	200	130	–	46.20	12.55		
	II-2	0.660	50	100	110	660	200	200	130	–	46.20	14.25		
	II-3	0.825	50	100	110	660	200	200	130	–	46.20	17.72		
	II-4	0.990	50	100	110	660	200	200	130	–	46.20	18.86		
	III-1	0.495	50	100	110	660	200	200	130	–	61.50	13.24		
	III-2	0.660	50	100	110	660	200	200	130	–	61.50	15.17		
	III-3	0.825	50	100	110	660	200	200	130	–	61.50	18.86		
	III-4	0.990	50	100	110	660	200	200	130	–	61.50	19.03		
Ceroni and Pecce [28]	*C150_100_1	0.165	100	150	230	4800	150	400	150	30	29.88	18.97	0.667	0.190
	*C150_100_2	0.165	100	150	230	4800	150	400	150	30	29.88	16.51	0.667	0.165
	*C150_100_3	0.165	100	150	230	4800	150	400	150	30	29.88	14.26	0.667	0.143
	*C150_100_4	0.165	100	150	230	4800	150	400	150	30	29.88	15.10	0.667	0.151
	*C150_75_1	0.165	75	150	230	4800	150	400	150	30	29.88	14.40	0.500	0.192
	*C150_75_2	0.165	75	150	230	4800	150	400	150	30	29.88	12.96	0.500	0.173
	*C150_50_1	0.165	50	150	230	4800	150	400	150	30	29.88	9.80	0.333	0.196
	*C150_50_2	0.165	50	150	230	4800	150	400	150	30	29.88	6.00	0.333	0.120
	*C150_50_3	0.165	50	150	230	4800	150	400	150	30	29.88	7.00	0.333	0.140
	*C150_25_1	0.165	25	150	230	4800	150	400	150	30	29.88	6.00	0.167	0.240
	*C150_25_2	0.165	25	150	230	4800	150	400	150	30	29.88	3.70	0.167	0.148
	*C150_25_3	0.165	25	150	230	4800	150	400	150	30	29.88	5.80	0.167	0.232
	C100_100_1	0.165	100	100	230	4800	150	400	150	30	29.88	13.63		
	C100_100_2	0.165	100	100	230	4800	150	400	150	30	29.88	13.36		
	*C150_100_2L_1	0.330	100	100	230	4800	150	400	150	30	29.88	20.12	0.667	0.201
	*C150_100_2L_2	0.330	100	100	230	4800	150	400	150	30	29.88	19.87	0.667	0.199
	*C150_50_2L_1	0.330	50	100	230	4800	150	400	150	30	29.88	11.44	0.333	0.229
	*C150_50_2L_2	0.330	50	100	230	4800	150	400	150	30	29.88	9.97	0.333	0.199
	*C150_50_2L_3	0.330	50	100	230	4800	150	400	150	30	29.88	10.04	0.333	0.201
Subramaniam et al. [29]	*DS_2	0.167	20	152	230	3830	52	330	125	–	39.00	6.15	0.385	0.308
	*DS_3	0.167	20	152	230	3830	52	330	125	–	39.00	6.45	0.385	0.323
	*Test 12	0.167	22	152	230	3830	52	330	125	–	39.00	7.44	0.423	0.338
	*Test 13	0.167	22	152	230	3830	52	330	125	–	39.00	7.17	0.423	0.326

(*continued on next page*)

Appendix (*continued*)

Authors	Specimen #	FRP					Concrete prism					Load		
		t_f [mm]	b_f [mm]	l_b [mm]	E_f [GPa]	f_f [MPa]	b [mm]	l [mm]	h [mm]	h_c [mm]	f_{cm} [MPa]	F_{max} [kN]	b_f/b	F/b_f
	*Test 7	0.167	25	152	230	3830	52	330	125	–	39.00	8.65	0.481	0.346
	*Test 8	0.167	25	152	230	3830	52	330	125	–	39.00	6.89	0.481	0.276
Carloni et al. [46]	DS-S1	0.167	25	152	230	3830	125	330	125	–	35.00	8.04		
	DS-S2	0.167	25	152	230	3830	125	330	125	–	35.00	7.74		
	DS-S3	0.167	25	152	230	3830	125	330	125	–	35.00	7.01		
Carloni et al. [47]	DS-ST_1	0.167	25	152	230	3830	125	330	125	–	42.00	5.80		
	DS-ST_2	0.167	25	152	230	3830	125	330	125	–	42.00	6.30		
	DS-ST_3	0.167	25	152	230	3830	125	330	125	–	42.00	6.00		
Authors	25_1L	1.400	25	25	170	3100	150	300	120	30	32.59	4.13		
	25_2L	1.400	25	25	170	3100	150	300	120	30	32.59	3.70		
	50_1W	1.400	25	50	170	3100	150	300	120	30	32.59	7.57	0.167	0.303
	50_2W	1.400	50	50	170	3100	150	300	120	30	32.59	17.10	0.333	0.342
	100_1W	1.400	50	100	170	3100	150	300	120	30	32.59	27.48	0.333	0.550
	100_2W	1.400	100	100	170	3100	150	300	120	30	32.59	46.28	0.667	0.463
	150_1L	1.400	50	150	170	3100	150	300	120	30	32.59	28.35		
	150_2L	1.400	50	150	170	3100	150	300	120	30	32.59	25.18		
	150_3L	1.400	50	150	170	3100	150	300	120	30	32.59	21.54		
	200_1L	1.400	50	200	170	3100	150	300	120	30	32.59	27.54		
	200_2L	1.400	50	200	170	3100	150	300	120	30	32.59	26.88		
	200_3L	1.400	50	200	170	3100	150	300	120	30	32.59	25.64		

* Test performed to analyze the FRP width effect.
** Test performed to analyze the FRP bond length effect.

References

[1] Hollaway LC, Teng JG. Strengthening and rehabilitation of civil infrastructures using fiber-reinforced polymer (FRP) composites. Cambridge CB21 6AH, England: Woodhead Publishing Limited; 2008.
[2] Monti G, Nisticò N. Square and rectangular concrete columns confined by CFRP: experimental and numerical investigation. Mech Compos Mater 2008;44 (3):289–308.
[3] Foraboschi P. Shear strength computation of reinforced concrete beams strengthened with composite materials. Compos Mech Comput Appl 2012;3 (3):227–52.
[4] Foraboschi P. Predictive multiscale model of delayed debonding for concrete members with adhesively bonded external reinforcement. Compos Mech Comput Appl 2012;3(4):307–29.
[5] Foraboschi P, Vanin A. New methods for bonding FRP strips onto masonry structures: Experimental results and analytical evaluations. Compos Mech Comput Appl 2013;4(1):1–23.
[6] Yuan H, Teng JG, Seracino R, Wu ZS, Yao J. Full-range behavior of FRP-to-concrete bonded joints. Eng Struct 2004;26(5):553–65.
[7] Yao J, Teng JG, Chen JF. Experimental study on FRP-to-concrete bonded joints. Compos B Eng 2005;36(2):99–113.
[8] Suo Z, Hutchinson J. Steady-state cracking in brittle substrates beneath adherent films. Int J Solids Struct 1989;25(11):1337–53.
[9] Tanaka T. Shear resisting mechanism of reinforced concrete beams with CFS as shear reinforcement [Graduation thesis]. Japan: Hokkaido University; 1996.
[10] Maeda T, Asano Y, Sato Y, Ueda T, Kakuta Y. A study on bond mechanism of carbon fiber sheet. In: Proceedings of 3rd international symposium on non-metallic (FRP) reinforcement for concrete structures. Sapporo, Japan; 1997. p. 287–95.
[11] von Holzenkämpfer P. Ingenieurmodelle des verbundes geklebter bewehrung für betonbauteile [Dissertation]. Germany: Technische Universität Braunschweig; 1994.
[12] Neubauer U, Rostásy, FS. Design aspects of concrete structures strengthened with externally bonded CFRP plates. In: Proceedings of 7th international conference on structural faults and repairs, Edinburgh, Scotland; 1997. p. 109–18.
[13] Täljsten B. Defining anchor lengths of steel and CFRP plates bonded to concrete. Int J Adhes Adhes 1997;17(4):319–27.
[14] Yuan H, Wu Z, Yoshizawa H. Theoretical solutions on interfacial stress transfer of externally bonded steel/composite laminates. J Struct Mech Earthquake Eng JSCE 2001;18(1):27–39.
[15] Wu ZS, Yuan H, Niu H. Stress transfer and fracture propagation in different kinds of adhesive joints. J Eng Mech ASCE 2002;128(5):562–73.
[16] Chen JF, Yang ZJ, Holt GD. FRP or steel plate-to-concrete bonded joints: effect of test methods on experimental bond strength. Steel Compos Struct 2001;1 (2):231–44.
[17] Ghosh S, Ling Y, Majumdar B, Kim R. Interfacial debonding analysis in multiple fiber reinforced composites. Mech Mater 2000;32(10):561–91.
[18] Lu XZ, Teng JG, Ye LP, Jiang JJ. Bond-slip models for FRP sheets/plates bonded to concrete. Eng Struct 2005;27(6):920–37.
[19] Kushch VI, Shmegera SV, Brøndsted P, Mishnaevsky Jr L. Numerical simulation of progressive debonding in fiber reinforced composite under transverse loading. Int J Eng Sci 2011;49(1):17–29.
[20] Lu XZ, Jiang JJ, Teng JG, Ye LP. Finite element simulation of debonding in FRP-to-concrete bonded joints. Constr Build Mater 2006;20(6):412–24.
[21] Niu H, Wu Z. Numerical analysis of debonding mechanisms in FRP-strengthened RC beams. Comput Aided Civil Infrastruct Eng 2005;20 (5):354–68.
[22] CNR DT200. Istruzioni per la progettazione, l'esecuzione ed il controllo di interventi di consolidamento statico mediante l'utilizzo di compositi fibrorinforzati; 2013.
[23] CEB-FIP. Externally bonded FRP reinforcement for RC structures. Bulletin No. 14, 2001; fib.
[24] Monti G, Renzelli M, Luciani P. FRP adhesion in uncracked and cracked concrete zones. In: Proceedings of 6th international symposium on FRP reinforcement for concrete structure, Singapore, Singapore; 2003.
[25] Brosen K. Anchorage of externally bonded steel plates and CFRP laminates for the strengthening of concrete elements [Doctoral Thesis]. Belgium: University of Leuven; 2001.
[26] Lu XZ, Ye LP, Teng JG, Jiang JJ. Meso-scale finite element model for FRP sheets/plates bonded to concrete. Eng Struct 2005;27(4):564–75.
[27] Subramaniam KV, Carloni C, Nobile L. Width effect in the interface fracture during shear debonding of FRP sheets from concrete. Eng Fract Mech 2007;74 (4):578–94.
[28] Ceroni F, Pecce M. Evaluation on bond strength in concrete elements externally reinforced with CFRP sheets and anchoring devices. J Compos Constr 2010;14(5):521–30.
[29] Subramaniam KV, Carloni C, Nobile L. An understanding of the width effect in FRP-concrete debonding. Strain 2011;47(2):127–37.
[30] Neto P, Alfaiate J, Vinagre J. A three dimensional analysis of CFRP-concrete bond behaviour. Compos B Eng 2014;59:153–65.
[31] Chen JF, Pan WK. Three dimensional stress distribution in FRP-to-concrete bond test specimens. Constr Build Mater 2006;20(1–2):46–58.
[32] Ye F, Yao J. A 3D finite element study on the effect of FRP plate width on interfacial stress between FRP and concrete. Bull Sci Technol 2008;24:853–9.
[33] Xu T, He ZJ, Tang CA, Zhu WC, Ranjith PG. Finite element analysis of width effect in interface debonding of FRP plate bonded to concrete. Finite Elem Anal Des 2015;93(C):30–41.
[34] Biolzi L, Ghittoni C, Fedele R, Rosati G. Experimental and theoretical issues in FRP-concrete bonding. Constr Build Mater 2013;41:182–90.
[35] Peroni L. Rinforzo di elementi in calcestruzzo e muratura con FRP [MS thesis]. Politecnico di Milano, Milano, Italy, A.A. 2009–2010.
[36] Mittelstedt C, Becker W. Interlaminar stress concentrations in layered structures: Part I – a selective literature survey on the free-edge effect since 1967. J Compos Mater 2004;38(12):1037–61.
[37] Abaqus Theory manual, version 6.6; 2006.
[38] Nakaba M, Kanakubo T, Furuta T, Yoshizawa H. Bond behavior between fiber-reinforced polymer laminates and concrete. ACI Struct J 2001;98 (3):359–67.
[39] Ferracuti B, Savoia M, Mazzotti C. Interface law for FRP-concrete delamination. Compos Struct 2007;80(4):523–31.

[40] Ortiz M, Pandolfi A. Finite-deformation irreversible cohesive elements for three-dimensional crack-propagation analysis. Int J Numer Methods Eng 1999;44(9):1267–82.
[41] Bocciarelli M, Colombi P, Fava G, Poggi C. Interaction of interface delamination and plasticity in tensile steel members reinforced by CFRP plates. Int J Fract 2007;146(1–2):79–92.
[42] Bocciarelli M, Colombi P. Elasto-plastic debonding strength of tensile steel/CFRP joints. Eng Fract Mech 2012;85:59–72.
[43] Barbieri G, Biolzi L, Bocciarelli M, Cattaneo S. Pull out of FRP reinforcement from masonry pillars: experimental and numerical results. Compos B Eng 2015;69:516–25.
[44] Bizindavyi L, Neale KW. Transfer lengths and bond strengths for composites bonded to concrete. J Compos Constr 1999;3(4):153–60.
[45] Toutanji H, Saxena P, Zhao L, Ooi T. Prediction of interfacial bond failure of FRP-concrete surface. J Compos Constr 2007;11(4):427–36.
[46] Carloni C, Subramaniam KV, Savoia M, Mazzotti C. Expermental determination of FRP-concrete cohesive interface properties under fatigue loading. Compos Struct 2012;94(4):1288–96.
[47] Carloni C, Subramaniam KV. Investigation of sub-critical fatigue crack growth in FRP/concrete cohesive interface using digital image analysis. Compos B Eng 2013;51:35–43.